Astronomy & Astrophysics

The GJ 504 system revisited

Combining interferometric, radial velocity, and high contrast imaging data⋆

[illegible]

(Affiliations can be found after the references)

ABSTRACT

Context. [illegible] $M_{\rm Jup}$ [illegible]

Aims. [illegible]

Methods. [illegible]

Results. [illegible] 1 35 0 04 R [illegible] 162 4 $^{38}_{43}$ [illegible] 18 6 $^{43}_{38}$ [illegible] 21 2 [illegible] 4 0 1 8 [illegible] $T_{\rm e}$ 550 50 [illegible] log L L 6 15 0 15 [illegible] $T_{\rm e}$ [illegible] M 1 3 $^{0\,6}_{0\,3}$ $M_{\rm Jup}$ [illegible] M 23 $^{10}_{9}$ $M_{\rm Jup}$ [illegible] $M_{\rm Jup}$ [illegible]

Conclusions. [illegible]

Key words. [illegible]

[illegible]

1. Introduction

R 30 300)

H_2O CH_4

1000 T_e 3000 K.

T_e 800K

J K J H)

T_e

T_e 500 600 K.

0 08 pc;

4 $^{4\,5}_{1\,0}$ $M_{\rm Jup}$,

2. Observations

2.1. SPHERE high-contrast observations

Table 1.

				DIT	NDIT	N_{EXP}					
				8	16	s	8	4	1	1	
				4	16	s	2	2	1	1	
				4	16	s	56	16	16	16	
				4	16	s	2	2	1	1	
				8	16	s	8	4	1	1	
				0	84	2 s	16	8	1	1	
				16	16	s	2	2	1	1	
				16	16	s	16	16	16	16	
				16	16	s	2	2	1	1	
				0	84	2 s	16	8	1		
				0	84	2 s	16	8	1		
				16	16	s	2	2	1	1	
				16	16	s	16	16	1	1	
				16	16	s	2	2	1	1	
				0	84	2 s	16	8	1	1	
				4	s	15	1				
				2	s	3	1				
				2	s	40	64				
				2	s	3	1				
				2	s	3	1				
				4	s	15	1				
				4	s	15	1				
				8	s	3	1				
				8	s	32	16				
				8	s	3	1				
				4	s	15	1				
				8	16	s	21	11	1	1	
				32	32	s	4	4	26	26	
				8	16	s	21	11	1	1	
				8	16	s	21	11	1	1	
				32	32	s	4	4	28	28	
				8	16	s	21	11	1	1	

Notes.

N_{EXP}

*Y*3 *J*3 *H*2, *K*1

*Y*2 *J*2 *H*3, *K*2

*Y*2 (*Y* 2 16 71 0 16

S/N

*H*3

*H*3

4 5

*J*2 *K*2

2

3

J H K L

1

2

Table 2. [illegible]

[illegible]	[illegible]	[illegible]	[illegible]	[illegible]	[illegible]	[illegible]				
[illegible]	[illegible]	H	9 500	0 005	0 35	0 02	2479	16	327 94	0 39
[illegible]	[illegible]	H	9 500	0 005	0 35	0 02	2483	8	327 45	0 19
[illegible]	[illegible]	L	20 54	0 03	0 28	0 09	2481	33	326 84	0 94
[illegible]	[illegible]	K_s	9 500	0 005	0 35	0 02	2483	15	326 46	0 36
[illegible]	[illegible]	J	9 500	0 005	0 35	0 02	2487	8	326 54	0 18
[illegible]	[illegible]	L	20 54	0 03	0 28	0 09	2499	26	326 14	0 61
[illegible]	[illegible]	$H2$	12 255	0 009	1 712	0 063	2491	3	323 46	0 07
[illegible]	[illegible]	$H2$	12 255	0 009	1 712	0 063	2496	3	323 50	0 07
[illegible]	[illegible]	$K1$	12 267	0 009	1 712	0 063	2497	4	323 60	0 10
[illegible]	[illegible]	$Y2$	12 283	0 009	1 712	0 063	2495	5	323 50	0 14
[illegible]	[illegible]	$Y3$	12 283	0 009	1 712	0 063	2501	3	323 49	0 07
[illegible]	[illegible]	$J3$	12 261	0 009	1 712	0 063	2499	6	323 40	0 14
[illegible]	[illegible]	$H2$	12 255	0 009	1 78	0 08	2495	2	322 48	0 05
[illegible]	[illegible]	$H3^a$	12 255	0 009	1 78	0 08	2493	12	322 83	0 32
[illegible]	[illegible]	$H2$	12 255	0 009	1 719	0 056	2493	3	321 74	0 08

Notes. [illegible] [illegible] [illegible] $^{(a)}$ [illegible]

Table 3. [illegible]

[illegible]	λ_c (μm)	(μm)	[illegible]	[illegible] (W m	[illegible] 1	[illegible] 1 ^{2} m ^{1})	(W m ^{2} m ^{1})	[illegible] (W m ^{2} m ^{1})	[illegible]	
Y2	[illegible]	[illegible]	[illegible]	[illegible]	[illegible]	[illegible]				
Y3	[illegible]	[illegible]	[illegible]	[illegible]	[illegible]	[illegible]				
J2	[illegible]	...			...	...	[illegible]	[illegible]		
J3	[illegible]	[illegible]	[illegible]	[illegible]	[illegible]	[illegible]				
H2	[illegible]	[illegible]	[illegible]	[illegible]	[illegible]	[illegible]				
H3 ^{a}	[illegible]	[illegible]	[illegible]	[illegible]	[illegible]	[illegible]				
K1	[illegible]	[illegible]	[illegible]	[illegible]	[illegible]	[illegible]				
K2	[illegible]		[illegible]	...	...	...	[illegible]	[illegible]		
J	[illegible]	[illegible]	[illegible]	[illegible]	[illegible]				[illegible]	[illegible]
H	[illegible]	[illegible]	[illegible]	[illegible]	[illegible]				[illegible]	[illegible]
K$_s$	[illegible]	[illegible]	[illegible]	[illegible]	[illegible]				[illegible]	[illegible]
CH$_4$S	[illegible]	[illegible]	[illegible]	[illegible]	[illegible]				[illegible]	[illegible]
CH$_4$L	[illegible]		[illegible]	...	...	...	[illegible]		[illegible]	[illegible]
L	[illegible]	[illegible]	[illegible]	[illegible]	[illegible]				[illegible]	[illegible]
[illegible]	[illegible]	[illegible]	[illegible]	[illegible]					[illegible]	[illegible]
[illegible]	[illegible]	[illegible]	[illegible]	[illegible]					[illegible]	[illegible]
[illegible]	[illegible]	[illegible]	[illegible]	[illegible]					[illegible]	[illegible]

Notes. [illegible] $J2$ [illegible] $K2$ [illegible] $^{(a)}$ [illegible]

2.2. Radial velocity

[illegible] R [illegible] sin i [illegible] 6 6 5 1 [illegible] ^{1}, [illegible] 1 [illegible] ^{1}) [illegible] ^{1} [illegible]

[illegible]

2.3. Interferometry

[illegible]

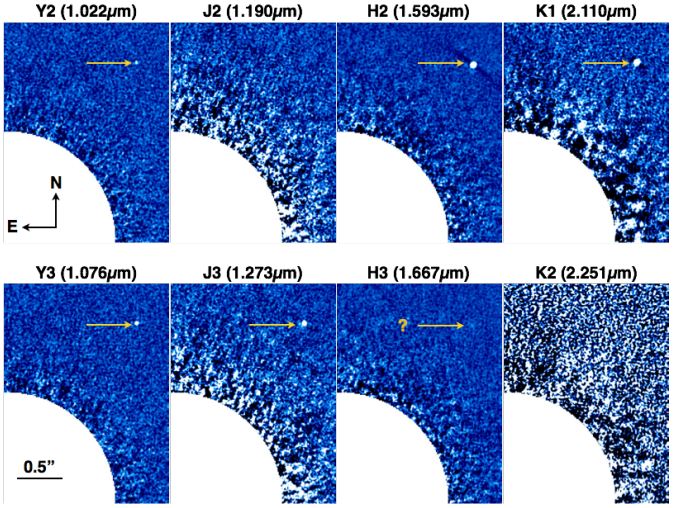

Fig. 1.

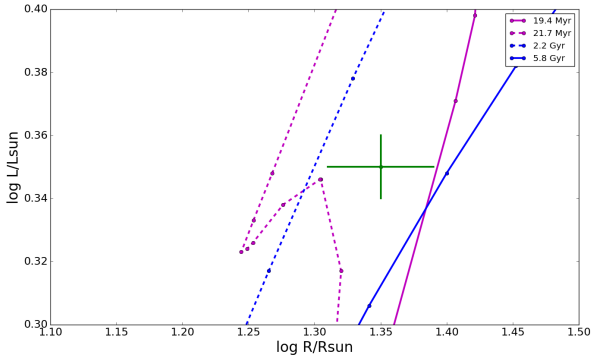

Fig. 2.

3. Revised stellar properties

(L_x L_{bol} 4 42 R_{HK} T_e M 0 01 0 04; 0 43 0 01; 160 $^{70}_{60}$ Y J H, K $Y3$ $Y2$ $Y3$ $J3$ $J3$ $H2$, $Y3$ $H2$ $J3$ $H2$ $H3$ $_4$ J H $J2$ $J3$ $H2$ $H3$, $K1$ $K2$ $K1$ $_2$ 3

Table 4.

	21	2	4 0	1 8	

4. Empirical analysis of GJ 504b photometry

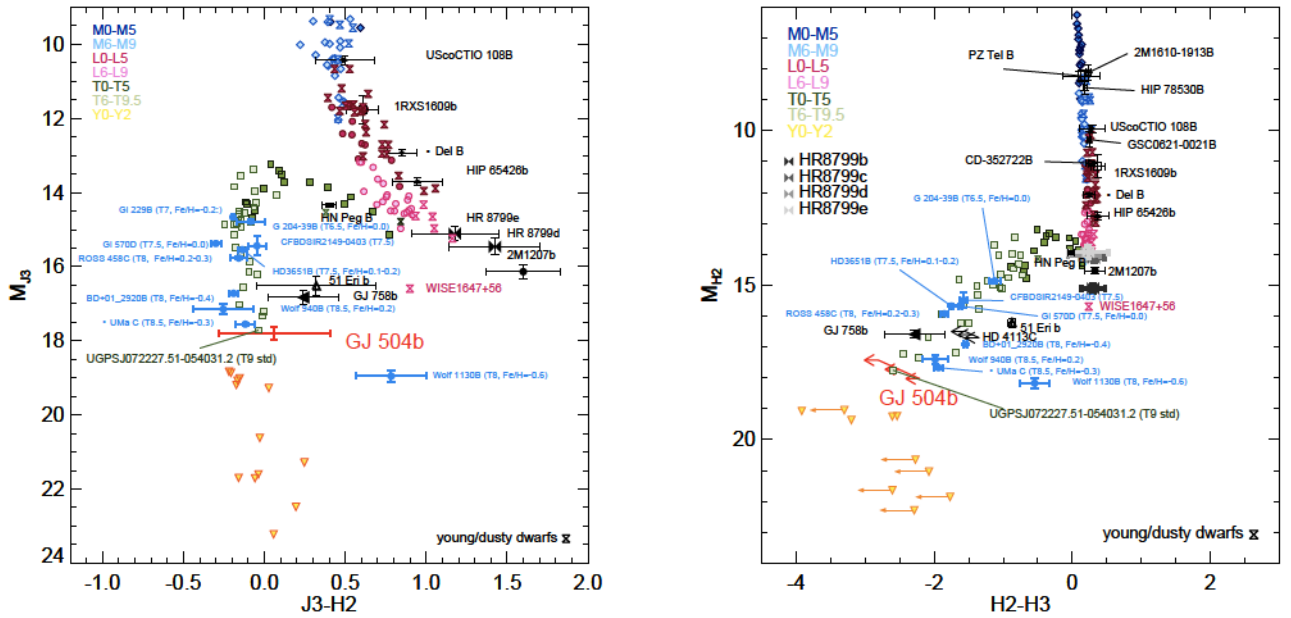

Fig. 3. Color-magnitude diagrams for the SPHERE/IRDIS photometry. The benchmark T-type companions are overlaid (full blue symbols). Their properties are summarized in Appendix B.

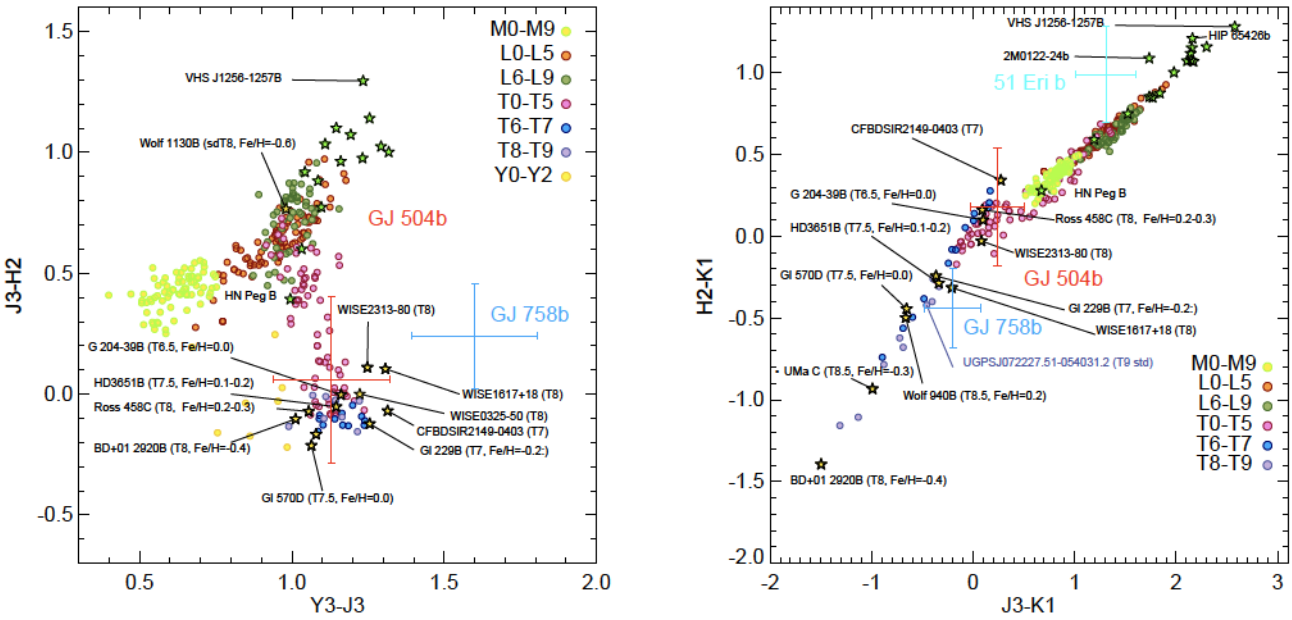

Fig. 4. Color–color diagram using the SPHERE/IRDIS photometry. The green stars correspond to dusty and/or young dwarfs at the L/T transition. The yellow stars correspond to the benchmark T-type companions and isolated objects listed in Table A.2.

planet 51 Eri b is orbiting a young star (Montet et al. 2015) and is proposed to be metal-enriched (Samland et al. 2017). Those objects confirm that the gravity and/or the metallicity induces a shift toward redder colors in that CCD.

We used the G goodness-of-fit indicator (Cushing et al. 2008) to compare the photometry of GJ 504b to those of reference objects (Fig. 5).

$$G_k = \sum_{i=1}^{n} w_i \left(\frac{f_i - \alpha_k F_{k,i}}{\sigma_i} \right)^2, \quad (1)$$

where f and σ are the observed photometry of GJ 504b and associated error, and w are the filter widths. F_k corresponds to the photometry of the template spectrum k. α_k is a multiplicative factor between the companion photometry and the one of the template which minimizes G_k.

The exclusion of the K-band photometry from the fit allows the comparison to be extended to the Y dwarf domain where the K band flux of those objects is fully suppressed. The reference photometry is taken from the SpeXPrism library (Burgasser 2014) in addition to Cushing et al. (2014), Mace et al. (2013a), and Schneider et al. (2015). We also added the photometry of peculiar late-T dwarfs described in Appendix B. Figure 6 provides a visual comparison of the fit for some objects of interest. We confirm that the overall NIR luminosity of the companion is best represented by the T9 standard UGPSJ072227.51-054031.2 (Lucas et al. 2010). Companions with super-solar metallicity and/or cloudy atmospheres tend to have reduced

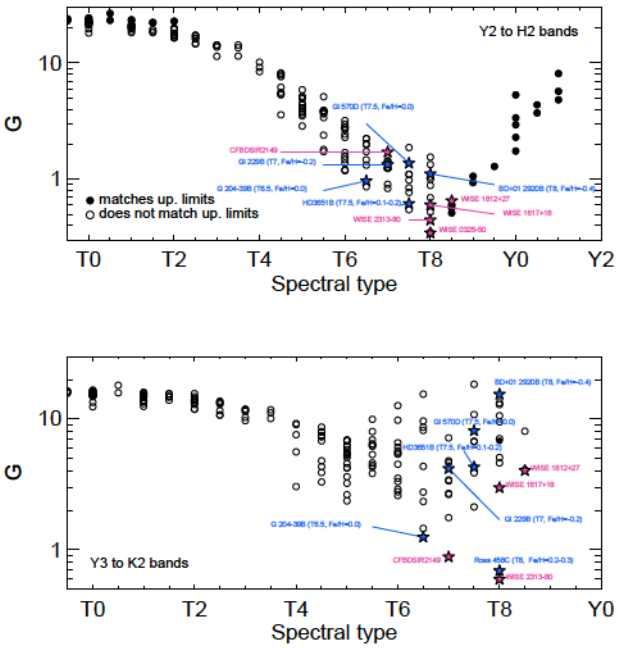

Fig. 5. Goodness-of-fits (G) corresponding to the comparison of GJ504b photometry to those of empirical objects in the $Y2$ to $H2$ bands (top) and from the $Y3$ to $K2$ bands (bottom). The blue stars correspond to benchmark T-type companions while the pink ones correspond to peculiar free-floating T-type objects (see Appendix B).

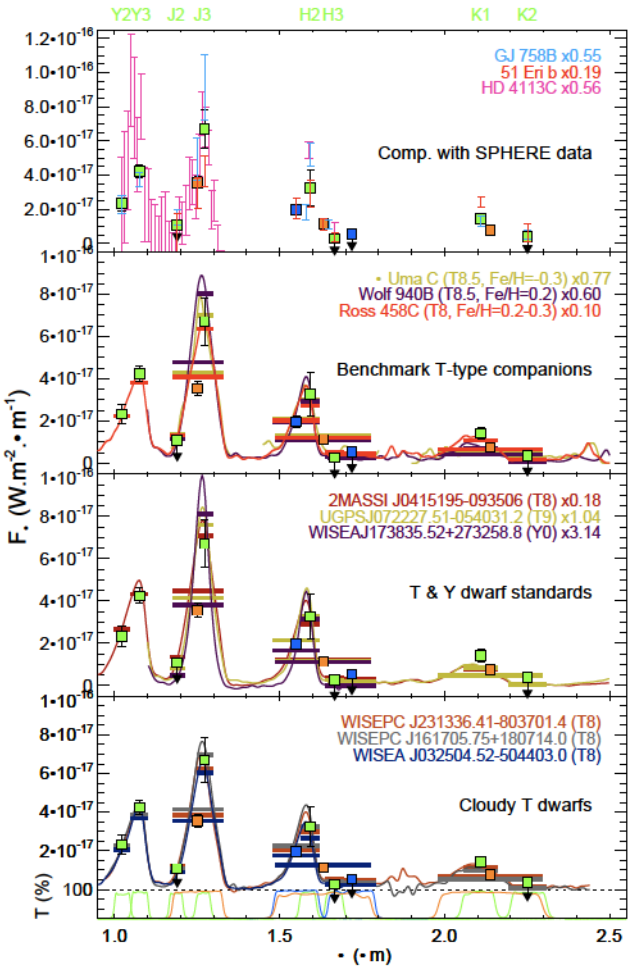

Fig. 6. Visual comparison of the SED of GJ 504b (green squares) to that of T-type companions observed with VLT/SPHERE, of benchmark companions with various metallicities, and of cloudy T dwarfs. The laying bars correspond to the flux of the template spectra averaged over the filter passbands whose transmission is reported at bottom.

G values compared to analogs with depleted metals. The T8 dwarf WISEA J032504.52–504403.0 produces the best fit of the YJH band flux; it is estimated to have a 100% cloudy atmosphere with low surface gravity (log g = 4.0) and be on the younger end of the age range (0.08–0.3 Gyr) of all considered objects in Schneider et al. (2015). The intermediate age and metal-rich companion ROSS 458C produces an excellent fit of the Y- to K-band fluxes of GJ 504b, but it is clearly more luminous.

We conclude that GJ 504b is a $T9^{+0.5}_{-1}$ object with peculiar NIR colors that could be attributed to low surface gravity and/or enhanced metallicity. We use atmospheric models in the following section to further explore this latter findings.

Using the $BC_J = 2.0^{+0.4}_{-0.1}$ mag and $BC_H = 1.7^{+0.4}_{-0.2}$ mag of $T9^{+0.5}_{-1}$ dwarfs from Dupuy & Kraus (2013), we find a log $(L/L_\odot) = -6.33^{+0.12}_{-0.20}$ and a log $(L/L_\odot) = -6.30^{+0.14}_{-0.22}$ for GJ 504b, respectively[6]. The bolometric corrections might however not be appropriate for the peculiar SED of GJ 504b because it corresponds to the averaged values for "regular" dwarfs in spectral type bins. Therefore, we considered the log $(L/L_\odot) = -6.20 \pm 0.03$ of the T9 object UGPS J072227.51-054031.2 (Dupuy & Kraus 2013) and the flux-scaling factor $\alpha = 1.04$ value found above to estimate a log $(L/L_\odot) = -6.18 \pm 0.03$ dex for GJ 504b . If the T8.5 companion Wolf 940B is used instead (log $(L/L_\odot) = -6.01 \pm 0.05$; Leggett et al. 2010), we find a log $(L/L_\odot) = -6.23 \pm 0.05$ dex for GJ 504b.

5. Atmospheric properties of GJ 504b

5.1. Forward modeling with the G statistics

5.1.1. Model description

We considered five independent grids of synthetic spectra relying on different theoretical models to characterize the atmospheric properties of the companion and to show differences in the retrieved properties related to the model choice. The grid properties are summarized in Table 5. We provide a succinct description of the atmospheric models below.

We used the model grid of the Santa Cruz group (hereafter the "Morley" models). The grid was previously compared to the GJ 504b SED (Skemer et al. 2016). It explores the case of metal-enriched atmospheres. These 1D radiative-convective equilibrium atmospheric models are similar to those described in Morley et al. (2012, 2014). They use the ExoMol methane line lists (Yurchenko & Tennyson 2014). The wings of the pressure-broadened KI and NaI bands in the optical can extend into the NIR in Y and J bands and are known to affect the modeling of T-dwarf spectra. In those models, the broadening is treated following Burrows et al. (2000). The models consider the improved treatment of the collision-induced absorption (CIA) of H_2 (Richard et al. 2012). They consider chemical equilibrium only, and account for the formation of resurgent clouds at the T/Y transition made of Cr, MnS, Na_2S, ZnS, and KCl particles. The cloud structure and opacities are computed following Ackerman & Marley (2001). The clouds are parametrized by the sedimentation efficiency (f_{sed}) which represents the balance between the upward transport of vapor and condensate by turbulent mixing in the atmosphere with the downward transport of

[6] Using $M_{bol,\odot}$ = 4.74 mag (Prša et al. 2016).

Table 5.

T_e (K)					[a]
log g (cgs)					
[M/H]	0				
K_{zz} (cm^2 s^{-1})	...	...	10^6	...	$10^{6.5}$, $10^{7.5}$, $10^{8.5}$
f_{sed}	...		inf	...	[b]
f_{cloud}	0	0	0	0	0
	...	...		...	...

Notes. [a] K_{zz} $10^{7.5}$ f_{sed} 2 0. [b] f_{sed} K_{zz} $10^{6.5}$ f_{sed} K_{zz} $10^{7.5}$ T_e

f_{sed}

g M H])

$_4$, O $_2$,
N $_2$ N $_3$.

$_4$ K N

H$_2$O $_4$, O $_2$, C $_2$H$_2$, H $_2$S H $_2$, N N $_3$, H
P H $_3$, H $_2$ H $_2$
$_4$

f_{sed}. K_{zz} H_p, K_{zz}
H_p

K_{zz}
$10^{7.5}$ cm^2 s^{-1} K_{zz}
$10^{8.5}$ cm^2 s^{-1} f_{sed} K_{zz} $10^{6.5}$ cm^2 s^{-1}
f_{sed} $_2$

T_e
$_2$ $_2$, $_4$,
CO $_2$, N $_3$, P $_3$,

$_3$,

K_{zz}
$_2$

F_{total} F_{clear} F_{cloudy}

(1 f_{cloud}) F_{clear} f_{cloud} F_{cloudy}

f_{cloud}
T_e, , [M H], f_{cloud}

5.1.2. Results

Table 6. [illegible]

T_e (K)	[illegible]	[illegible]	[illegible]	[illegible]	[illegible]
log (g cm s^{-2})	[illegible]	[illegible]	[illegible]	[illegible]	[illegible]
[M/H] (dex)	[illegible]	[illegible]	[illegible]	[illegible]	[illegible]
K_{zz} (cm^2 s^{-1})	[illegible]	[illegible]	[illegible]	[illegible]	[illegible]
f_{sed}	[illegible]	[illegible]	[illegible]	[illegible]	[illegible]
f_{cloud}	[illegible]	[illegible]	[illegible]	[illegible]	[illegible]
[illegible]	[illegible]	[illegible]	[illegible]	[illegible]	[illegible]
R (R_{Jup})	[illegible]	[illegible]	[illegible]	[illegible]	[illegible]
M (M_{Jup})	[illegible]	[illegible]	[illegible]	[illegible]	[illegible]
log (L/$L_\odot$)	[illegible]	[illegible]	[illegible]	[illegible]	[illegible]
G	[illegible]	[illegible]	[illegible]	[illegible]	[illegible]
T_e (K)	[illegible]	[illegible]	[illegible]	[illegible]	[illegible]
log (g cm s^{-2})	[illegible]	[illegible]	[illegible]	[illegible]	[illegible]
[M/H] (dex)	[illegible]	[illegible]	[illegible]	[illegible]	[illegible]
K_{zz} (cm^2 s^{-1})	[illegible]	[illegible]	[illegible]	[illegible]	[illegible]
f_{sed}	[illegible]	[illegible]	[illegible]	[illegible]	[illegible]
f_{cloud}	[illegible]	[illegible]	[illegible]	[illegible]	[illegible]
[illegible]	[illegible]	[illegible]	[illegible]	[illegible]	[illegible]
R (R_{Jup})	[illegible]	[illegible]	[illegible]	[illegible]	[illegible]
M (M_{Jup})	[illegible]	[illegible]	[illegible]	[illegible]	[illegible]
log (L/$L_\odot$)	[illegible]	[illegible]	[illegible]	[illegible]	[illegible]
G	[illegible]	[illegible]	[illegible]	[illegible]	[illegible]

Notes. [illegible]

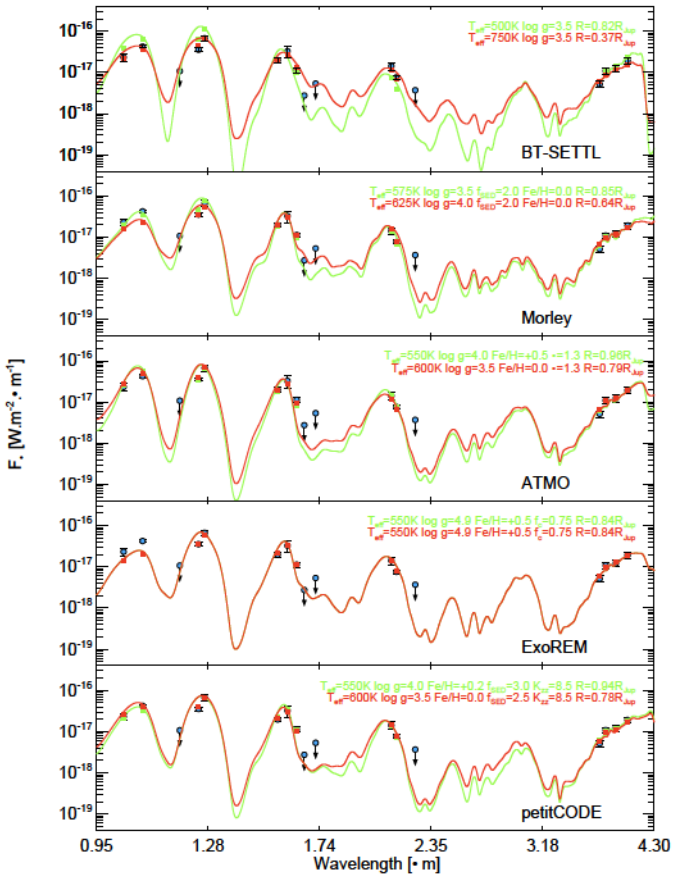

Fig. 7. Best-fitting model spectra when using the G statistics. Solutions with some pre-requisite on the object radius are shown in green. The solutions without any constraints on the object radius are shown in red. The GJ 504b's photometry is overlaid as blue dots.

cover provide the best fit of all considered models. In addition, the **ATMO** models which do consider the thermo-chemical instability as an alternative to cloud formation yield G values lower than those of the Exo-REM models. Therefore, additional data are needed to comment on the occurrence of clouds in the atmosphere of GJ 504b (see Sect. 8.2).

Several indications in the fitting solution based on the G statistics confirm the peculiarity of GJ 504b atmosphere:

- All but the Exo-REM models provide a best fit for low surface gravities. The evolution of G with log g indicates that this parameter is well constrained by the Morley, **ATMO**, and **petitCODE** grids. This is not the case however for the two other models. Burgasser et al. (2011) and Schneider et al. (2015) find surface gravities in the same range as GJ 504b for the cloudy T8 objects WISEPC J231336.41-803701.4, WISEA J032504.52-504403.0, and ROSS 458C. Our values are also consistent with those found for 51 Eri b (Samland et al. 2017; Rajan et al. 2017).
- The **petitCODE** and Morley cloudy models find $f_{\rm sed}$ in the range 2–3. These values are lower than the ones found for WISEA J032504.52-504403.0 when using models from the Santa-Cruz group (Schneider et al. 2015). They are higher, however, than the one derived with the **petitCode** models for 51 Eri b (using the SPHERE spectrum; Samland et al. 2017), but are consistent with the $f_{\rm sed}$ quoted for 51 Eri b using the Morley model grid (Rajan et al. 2017). Those $f_{\rm sed}$ values are lower than those found for old late-T objects and consistent with the low surface gravities found.
- The **petitCODE** models favor solutions with high K_{zz} values ($10^{8.5}$ cm^2 s^{-1}). K_{zz} enters by setting the cloud particle size (together with $f_{\rm sed}$) in **petitCODE**. The solution also corresponds to the largest $f_{\rm sed}$ values available in the grid. This can be interpreted as a need for models with reduced cloud opacity rather than intense vertical mixing. The K_{zz} value of GJ 504b is well above (10^4–10^6 cm^2 s^{-1}) the one determined for the companion Wolf 940B (Leggett et al. 2010). Wolf 940A has the same metallicity ($[M/H] = +0.24 \pm 0.09$) as GJ 504A. But the Wolf 940 system is clearly old (3–10 Gyr).
- The best fit with the Morley grid corresponds to a model with $[M/H] = 0$. This is at odds with the conclusions from Skemer et al. (2016) found with the same model grid. We discuss the disagreement below.

We explore in the following section the degeneracies between the free parameters of the models.

5.2. Evaluating the degeneracies

We ran Markov-chain Monte-Carlo (MCMC) simulations of GJ 504b photometry for the most regular grids (Morley and **petitCODE**) of models to explore the posterior probability distribution for each model free parameter, and to evaluate the degeneracies between the different parameters. Each datapoint was considered with an equal weight in the likelihood function. The radius is left to evolve freely during the fit. We used the python implementation of the **emcee** package (Goodman & Weare 2010; Foreman-Mackey et al. 2013) to perform the MCMC fit of our data. The convergence of the MCMC chains is tested using the integrated autocorrelation time (Goodman & Weare 2010). Each MCMC step required a model to be generated for a set of free parameters that was not necessarily in the original model grid. We then performed linear re-interpolation of the grid of models in that case.

We coupled **emcee** to the Morley grid using a custom code (Vigan et al. in prep). Upper limits are accounted for in the fit as a penalty term in the calculation of the log-likelihood: if the predicted photometry of the model in a given filter is above the upper limit set by the observations, it is taken into account in the calculation of the likelihood; if it is below, it is not taken into account. We excluded the rained-out models ($f_{\rm sed} = +\infty$) beforehand. The posterior distributions are shown in Fig. 8. We estimate (1σ confidence level) $T_{\rm eff} = 559^{+25}_{-24}$ K, $\log g = 3.72^{+0.27}_{-0.16}$ dex, $[M/H] = 0.25 \pm 0.14$ dex, $f_{\rm sed} = 2.36^{+0.65}_{-0.37}$, and $R = 0.89^{+0.13}_{-0.11} R_{\rm Jup}$. The solution is in good agreement with the one found with the G statistics when R is constrained. The posteriors on $T_{\rm eff}$, log g, and $f_{\rm sed}$ are quite similar to those reported in Skemer et al. (2016) using a close MCMC approach and the same model grid. We nonetheless find a lower metallicity. Our value is in excellent agreement with the one determined for GJ 504A. This parameter is correlated with the $T_{\rm eff}$ and R. Skemer et al. (2016) set priors on R corresponding to a range of radii predicted by the "hot-start" evolutionary models. Adopting a flat prior on the radius in the range 0.82–1.26 $R_{\rm Jup}$ (see Sect. 5.1.2) does not modify our posteriors significantly. We find $T_{\rm eff} = 552^{+16}_{-20}$ K, $\log g = 3.72^{+0.28}_{-0.17}$ dex, $[M/H] = 0.27^{+0.14}_{-0.13}$ dex, $f_{\rm sed} = 2.40^{+0.66}_{-0.38}$, and $R = 0.93^{+0.11}_{-0.07} R_{\rm Jup}$. The analysis does not alleviate the correlation between the $f_{\rm sed}$ and log g values. The radius is more consistent with those of old brown dwarfs. The luminosity is in good agreement with the one determined empirically.

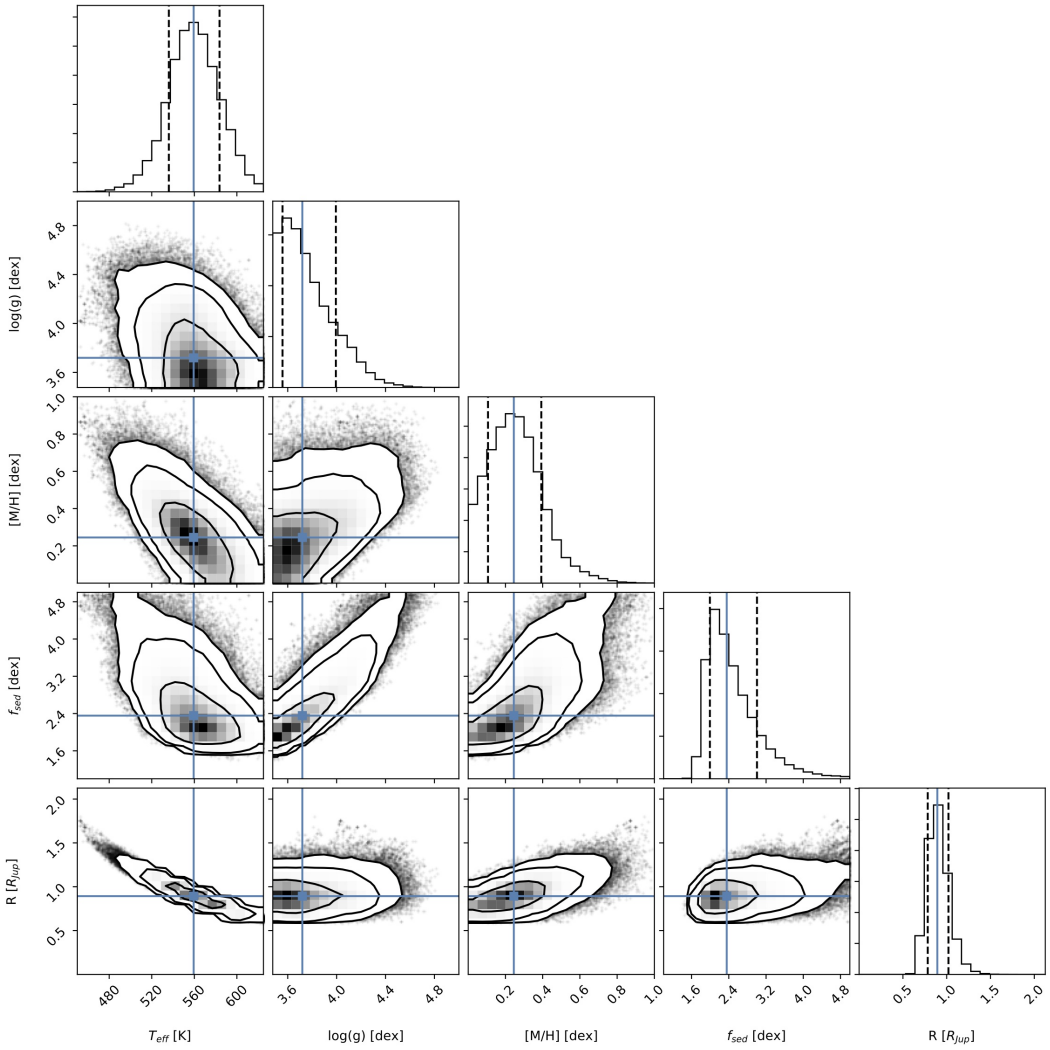
log(g) [dex]
[M/H] [dex]
f_{sed} [dex]
R [R_{Jup}]
T_{eff} [K]
log(g) [dex]
[M/H] [dex]
f_{sed} [dex]
R [R_{Jup}]

Fig. 8.

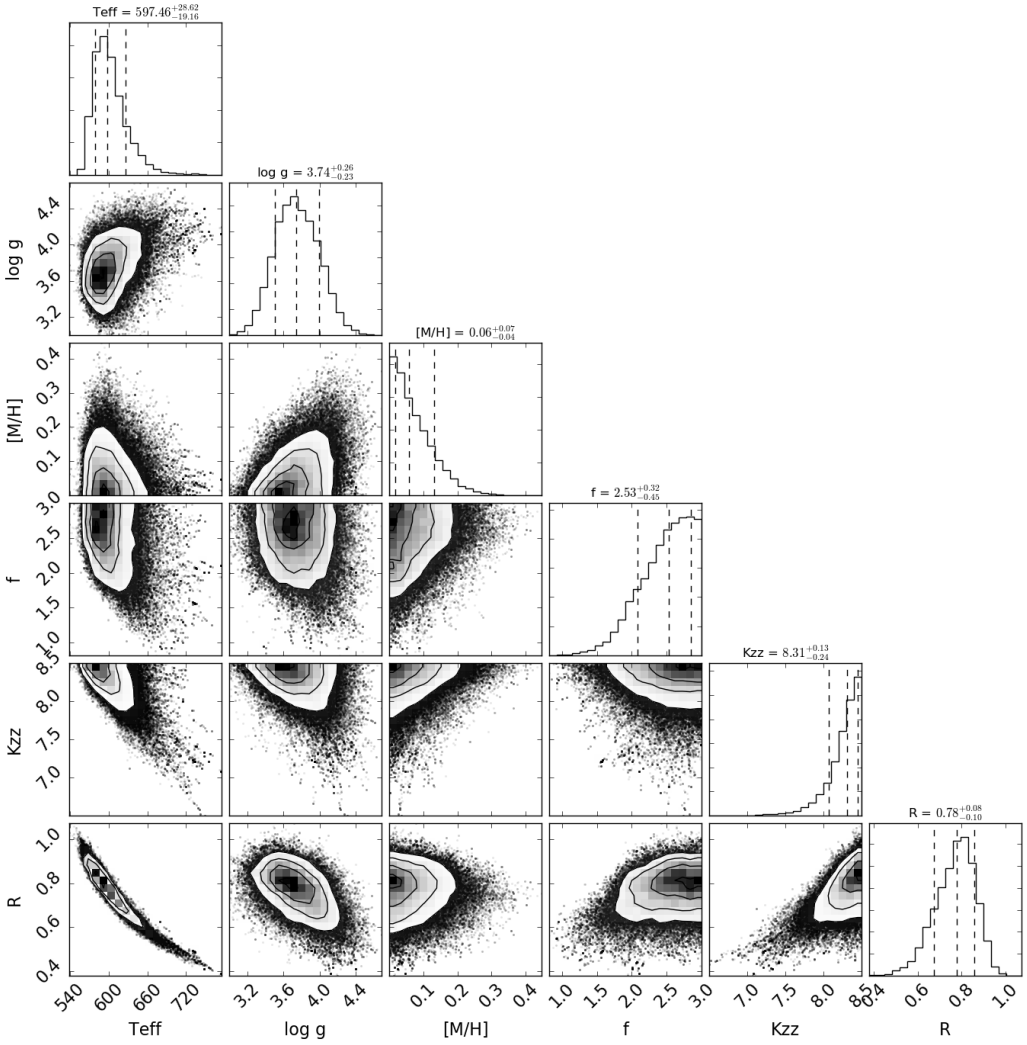

Fig. 9. [illegible]

[illegible] $[M/H]$ [illegible]

[illegible] [8] [illegible]

[illegible] $[M/H]$ [illegible]

[illegible] $M/H]$, [illegible] $T_{\rm e}$ [illegible]

[illegible] $\log(L/L_\odot)$ [illegible] $T_{\rm e}$ [illegible]

[8] [illegible]

6. Mass estimates

[illegible] [9].

[illegible] $S_{\rm init}$ [illegible]

[9] [illegible] $M_{\rm Jup}$.

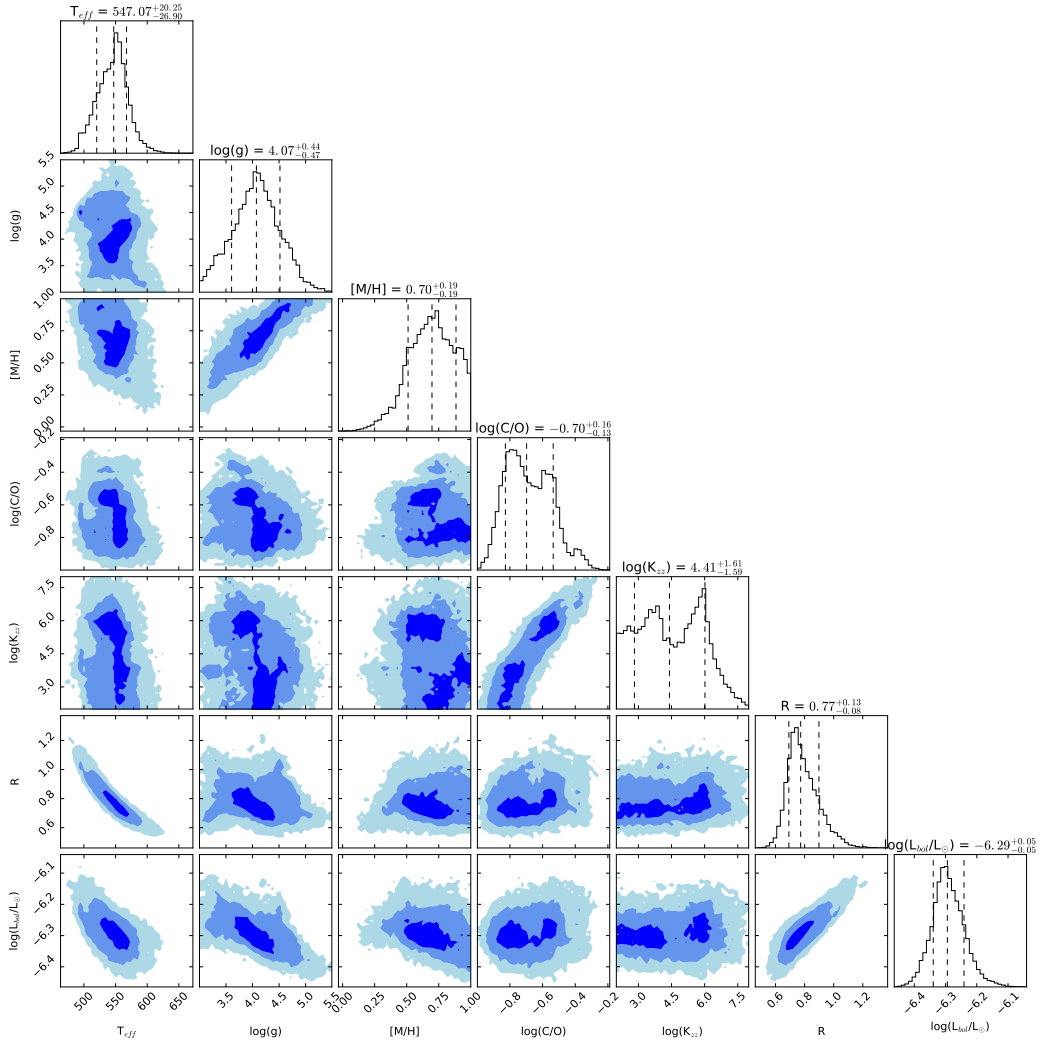

Fig. 10. [illegible]

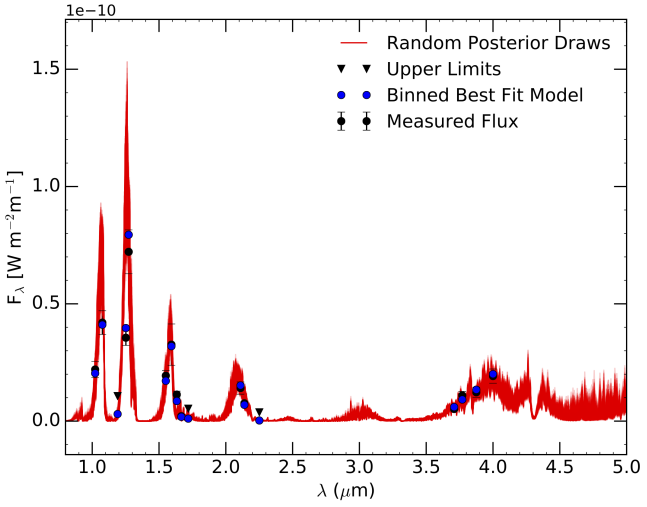

Fig. 11. [illegible]

[illegible] $M_{\rm Jup}$ [illegible] $M_{\rm Jup}$, [illegible] M

[illegible] $1\,3\,^{0\,6}_{0\,3}\,M_{\rm Jup}$ [illegible] M $1\,3\,^{1}_{0\,6}\,M_{\rm Jup}$ [illegible]

[illegible] $MS_{\rm init}$ [illegible]

[illegible] a M [illegible] 3 [illegible]

[illegible] $MS_{\rm init}$ [illegible]

[illegible] 2 M [illegible] a M [illegible] $MS_{\rm init}$ [illegible] $S_{\rm init}$ [illegible]

[illegible] 4 [illegible]

[illegible] $S_{\rm init}$ [illegible] $k_{\rm B}$ [illegible] $S_{\rm init}$ [illegible] M [illegible] $1\,3\,^{0\,4}\,M_{\rm Jup}$.

[illegible] 3

Table 7. "Hot-start" evolutionary model predictions.

		Saumon & Marley 2008 – no cloud – [M/H]=+0.3					COND03 – cloud free – 1x solar				
Age (Gyr)	Input	Mass (M_{Jup})	R (R_{Jup})	T_{eff} (K)	log g (dex)	log($L/L_\odot$) (dex)	Mass (M_{Jup})	R (R_{Jup})	T_{eff} (K)	log g (dex)	log($L/L_\odot$) (dex)
0.021 ± 0.002	T_{eff}	…	…	…	…	…	$2.5^{+0.6}_{-0.5}$	1.24 ± 0.01	…	3.61 ± 0.09	$-5.87^{+0.6}_{-0.5}$
0.021 ± 0.002	log($L/L_\odot$)	…	…	…	…	…	$1.7^{+0.5}_{-0.4}$	1.23 ± 0.01	470^{+43}_{-40}	$3.45^{+0.11}_{-0.10}$	…
4 ± 1.8	T_{eff}	$23.8^{+7.5}_{-8.1}$	$0.94^{+0.07}_{-0.05}$	…	$4.84^{+0.17}_{-0.24}$	−6.11 ± 0.18	$23.5^{+8.8}_{-6.2}$	$0.94^{+0.05}_{-0.06}$	…	$4.83^{+0.20}_{-0.17}$	$-6.15^{+0.16}_{-0.18}$
4 ± 1.8	log($L/L_\odot$)	$22.9^{+8.7}_{-8.6}$	$0.95^{+0.08}_{-0.06}$	537^{+68}_{-64}	$4.82^{+0.19}_{-0.27}$	…	$23.5^{+10.2}_{-6.7}$	$0.94^{+0.05}_{-0.06}$	550^{+69}_{-59}	$4.83^{+0.22}_{-0.18}$	…

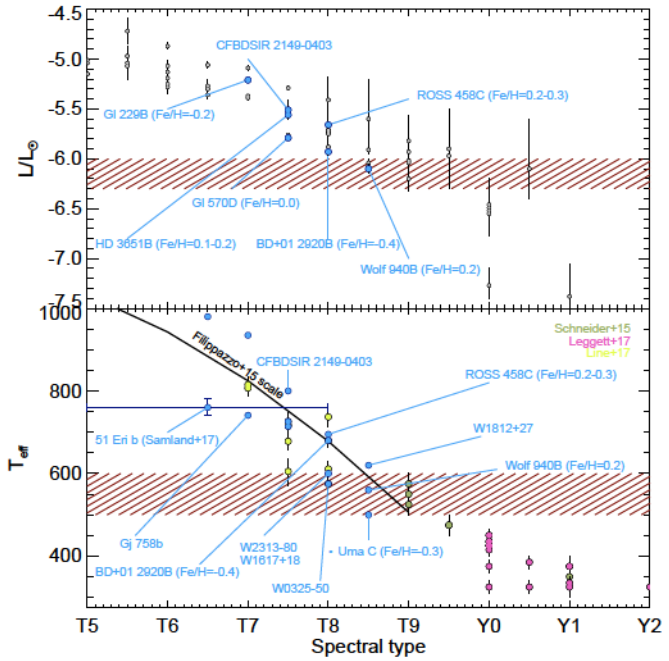

Fig. 12. Comparison of the final T_{eff} and bolometric luminosity of GJ 504b (dashed zone) to those of late-T and early-Y dwarfs. The bolometric luminosity values are taken from Dupuy & Kraus (2013) and Delorme et al. (2017a). The temperatures and luminosity of benchmark companions are taken from Table A.2. We added the T_{eff} determined by Leggett et al. (2017), Line et al. (2017), and Schneider et al. (2015) using atmospheric models and report the T_{eff}/spectral type conversion scale of Filippazzo et al. (2015).

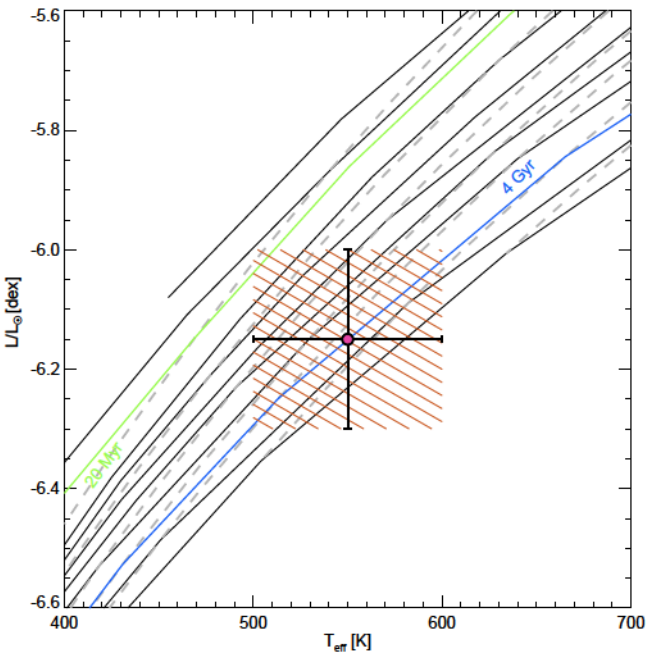

Fig. 13. Luminosity and T_{eff} of GJ 504b compared to the COND03 ("hot-start") evolutionary tracks. The solid lines correspond to the 5, 10, 20, 100, 300, 600 Myr and 1, 2, 4, 6, and 10 Gyr isochrones (*from top to bottom*). The dashed lines correspond to the model predictions for masses of 1, 5, 10, 15, 20, 30, and 40 M_{Jup} (*from top to bottom*).

7. Architecture

7.1. Companion orbit

We considered the astrometry reported in Table 2 as input of our MCMC orbit fitting packages to set constraints on the orbital parameters of GJ 504b. The code was developed for β Pictoris b and Fomalhaut b's orbits (Chauvin et al. 2012). We considered a mass of 1.2 $M_\odot$ for GJ 504A. We assume flat priors on log(P), e, cos(i), $\Omega + \omega$, $\omega - \Omega$, and T_p following Ford (2006). We ran ten chains in parallel and used the Gelman-Rubin statistics as convergence criterion (see details in Ford 2006).

The fit was performed on the whole set of epochs. We neglected the epoch from August 15, 2011 reported in Kuzuhara et al. (2013) for which the data were taken under poor conditions and the astrometry appears to be deviant. However, it is still possible that some systematic angular offsets between each instrument could have biased our analysis. We then also modeled the SPHERE epochs only, for comparison. The posteriors are shown in Fig. 15 for the two data sets. Figure 16 shows the correlation between the different posterior distributions of orbital parameters of GJ 504b when all the astrometric epochs are accounted for in the fit.

The posterior distributions do not change significantly when considering the homogeneous SPHERE data, or the data from all instruments. The accuracy of the SPHERE astrometry yields the most constraints on the orbital parameters and is therefore not heavily influenced by putative systematic errors on the HiCIAO and IRCS astrometry. We, therefore, considered the results from the whole set of epochs in the following. A sample of corresponding orbits is shown in Fig. 17. This shows that no curvature can be detected with the present astrometric monitoring.

The posterior on the semi-major axis points at 44 au which corresponds to the companion projected separation with 68% of the solutions in the range 44 ± 11 au. The fit excludes orbits with a semi-major axis shorter than ~27.8 au. The periods are significantly longer than the time span of the Lick and SOPHIE radial velocities and are likely to prevent us from obtaining constraints on the dynamical mass of GJ 504b.

The eccentricity is lower than 0.55 and peaks at 0.31 (e = 0.31 ± 0.15; 68% solutions). Our new data and fit do not yield solutions at higher eccentricity found by Kuzuhara et al. (2013). We find an inclination of $137.8^{+12.9}_{-4.6}$ degrees. There is no solution

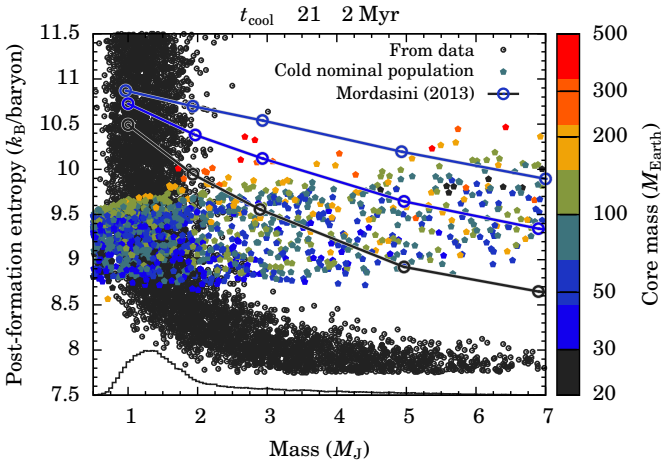

Fig. 14. [illegible] $S_{\rm init}$ 6 [illegible] $t_{\rm cool}$ 21 2 [illegible] log L L 6 15, [illegible] $M_{\rm core}$. [illegible] 9 $M_{\rm Earth}$ [illegible] *bottom to top*). [illegible] $MS_{\rm init}$ [illegible]

6 i 120 [illegible] 0 , [illegible] 1 M [illegible]

7.2. A spin-orbit misalignment?

[illegible] R [illegible] 3 [illegible] i [illegible]

$$i \quad \sin^{1} \frac{p}{2} \frac{P}{R}$$

[illegible] $_{\rm p}$ sin i [illegible] P [illegible]

$_{\rm p}$ 6 5 1 0 km s ^{1} [illegible]

[illegible] P 3 33 $^{0\ 08}_{0\ 10}$ [illegible] i

162 4 $^{3\ 8}_{4\ 3}$ [illegible] 18 6 $^{4\ 3}_{3\ 8}$ [illegible] [0] [illegible] i_c [illegible]

[illegible]

$$\cos^{1} \cos i \cos i_p \sin i \sin i_p \cos$$

[illegible]

[illegible] ^{1} [illegible] i_c

[illegible] i : i i i_c . [illegible] 0 [illegible] 8 [illegible] i [illegible] i [illegible] 10 [illegible]

7.3. Constraints on additional companions

[illegible] [illegible] $M_{\rm Jup}$ [illegible] 9 [illegible] 5 [illegible]

[illegible]

[illegible] ^{1} [illegible]

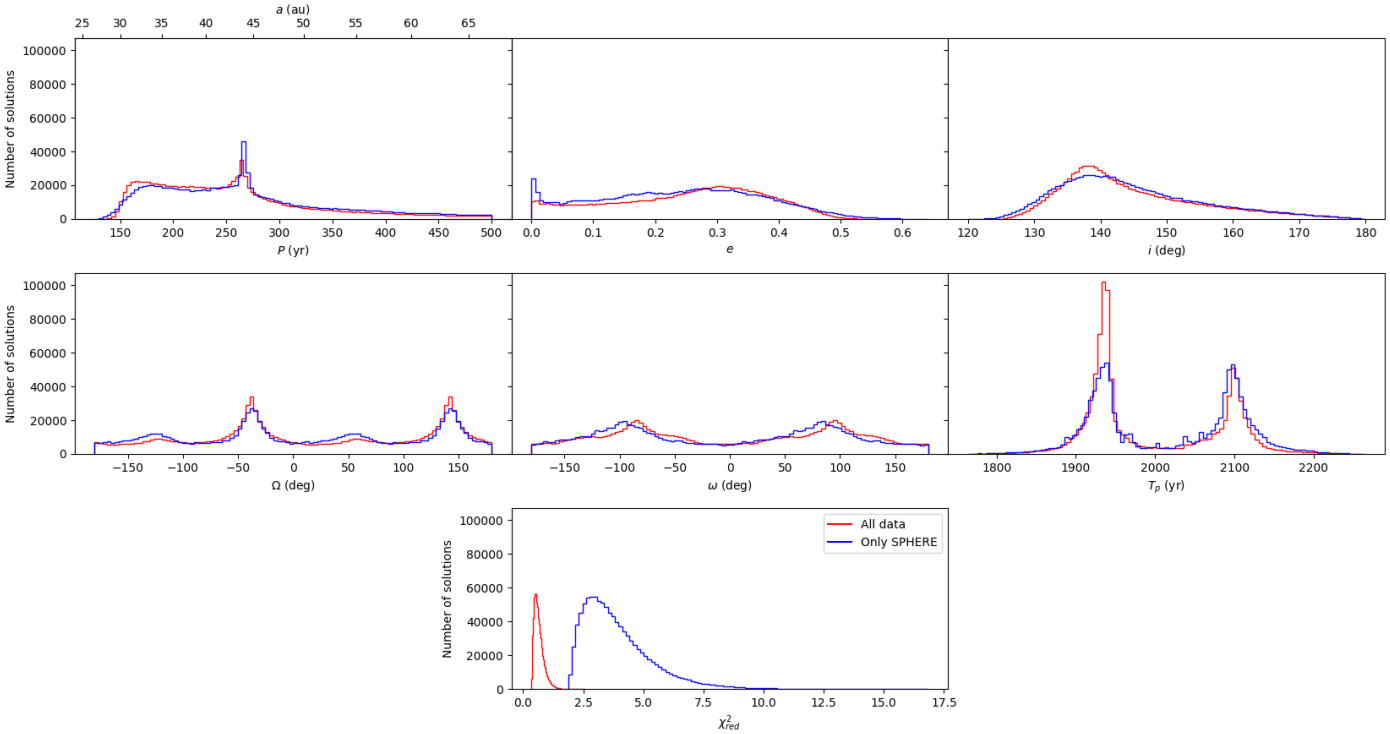
a (au)
Number of solutions
P (yr)
e
i (deg)
Ω (deg)
ω (deg)
T_p (yr)
All data
Only SPHERE
χ^2_{red}

Fig. 15. [illegible]

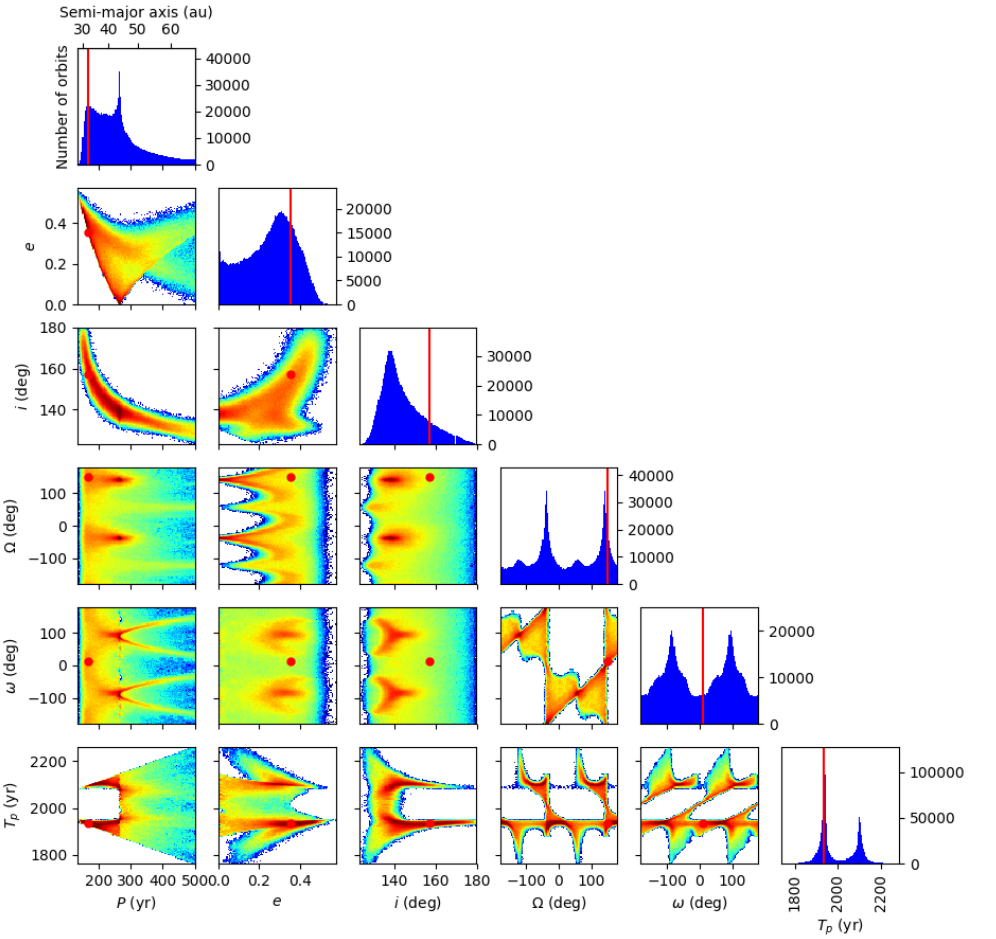
Semi-major axis (au)
Number of orbits
e
i (deg)
Ω (deg)
ω (deg)
T_p (yr)
P (yr)

Fig. 16. [illegible]

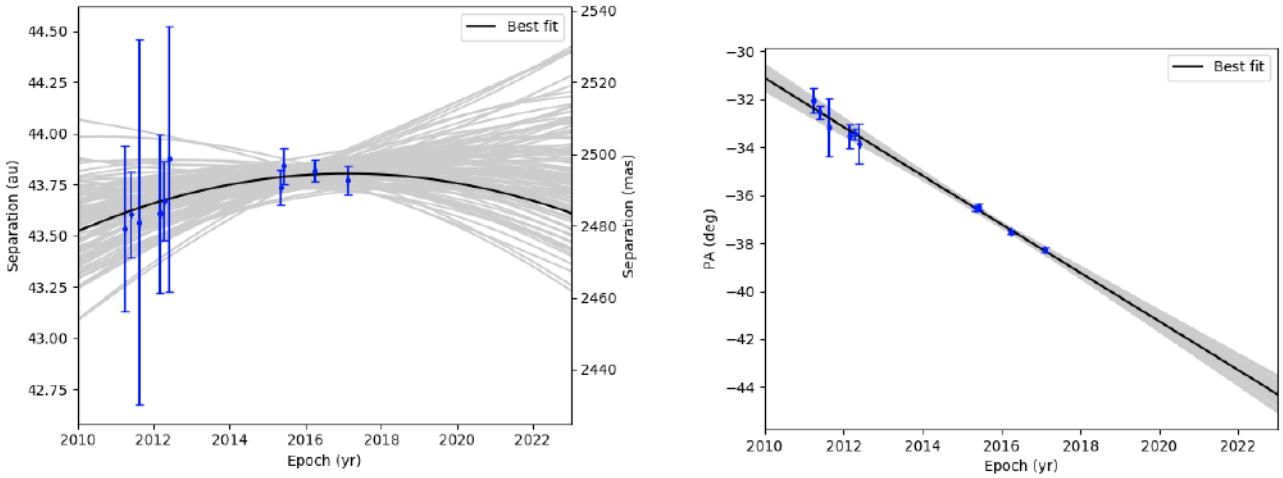

Fig. 17. Sample of 100 orbits obtained with the MCMC algorithm applied to GJ 504b astrometry (blue points).

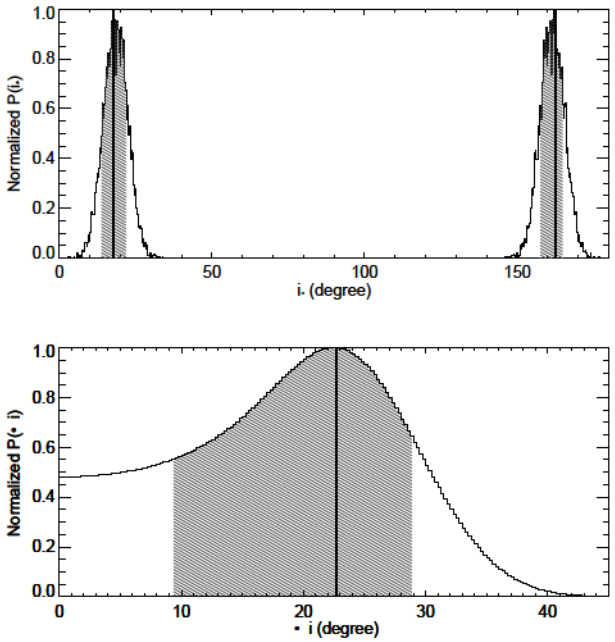

Fig. 18. *From top to bottom panels*: line-of-sight inclination $i_\star$ of GJ 504, and absolute difference between i_c and $i_\star$ when only $i_\star \geq 90°$ are considered. The dashed zones correspond to 68.28% of the solutions.

No object more massive than 2.5 $M_{\rm Jup}$ (apart GJ 504b) exists in the system assuming the young isochronal age. Our simulations reveal in addition that the Lick data (21.6 yr span) enable a more in-depth exploration of the separations from 0.2 to 6 au than the SOPHIE data (3.2 yr span). Both of the data sets give comparable constraints from 0.01 to 0.1 au.

8. Discussion

8.1. Conflicting age indicators

8.1.1. The planet engulfment scenario

Fuhrmann & Chini (2015) proposed that the engulfment of a jovian planet (2.7 $M_{\rm Jup}$) could have sped up GJ 504A's rotation velocity. D'Orazi et al. (2017b) estimate that the engulfment should have occurred no more than 200 Myr ago for the system to keep a sufficient imprint of the event on the star rotation speed. Such an engulfment may also enrich the host star in metals (Carlberg et al. 2012; Saffe et al. 2017).

In that case, what could have triggered the engulfment long after the dispersal of the circumstellar disk? Our detection limits indicate that no other companions more massive than the proposed engulfed planet are presently located in the first astronomical unit around GJ 504A. GJ 504b is likely the most massive object in the system, and therefore a good candidate perturber. The Lidov–Kozai mechanism (Kozai 1962; Lidov 1962) invoked by Fuhrmann & Chini (2015) and D'Orazi et al. (2017b) could only operate in the system if the obliquity φ of GJ 504b were higher than at least 40 deg. Additional astrometric monitoring of the companion is required to carve the distribution of relative inclinations Δi and provide a lower limit on φ. Two known systems have recently been discovered with close-in low-mass planets on eccentric orbits and more massive companions on wide-orbits: HD 219828 (Santos et al. 2016) and HD 4113 (Cheetham et al. 2018a). These systems might then be good proxies of the architecture of the GJ 504 system prior to the putative engulfment.

8.1.2. Effect of polar spots

Because GJ 504A is active and seen close to pole-on, high-latitude spots may be affecting the luminosity and $T_{\rm eff}$ estimates used for comparison to the tracks. These spots are predicted to occur on rapid rotators such as GJ 504A and young stars (Schuessler & Solanki 1992; Buzasi 1997; Schrijver & Title 2001; Holzwarth et al. 2006; Yadav et al. 2015). Observations of polar spots on active G-type stars might have been observed (e.g., Marsden et al. 2005, 2006, 2011; Waite et al. 2011, 2017). The polar spots (or cap) can fill up to 50% of the stellar surface and have lifetimes of about a decade.

Given a spot filling factor p (defined as $R_{\rm s}/R_\star^2$, where $R_{\rm s}$ is the spot radius), the observed luminosity $L_{\rm obs}$ of GJ 504A relative to the photosphere luminosity $L_{\rm phot}$ is

$$L_{\rm obs}/L_{\rm phot} = \frac{p \times T_{\rm spot}^4 + (1-p) \times T_{\rm phot}^4}{T_{\rm phot}^4}, \quad (5)$$

where $T_{\rm spot}$ is the spot temperature and $T_{\rm phot}$ the photosphere temperature.

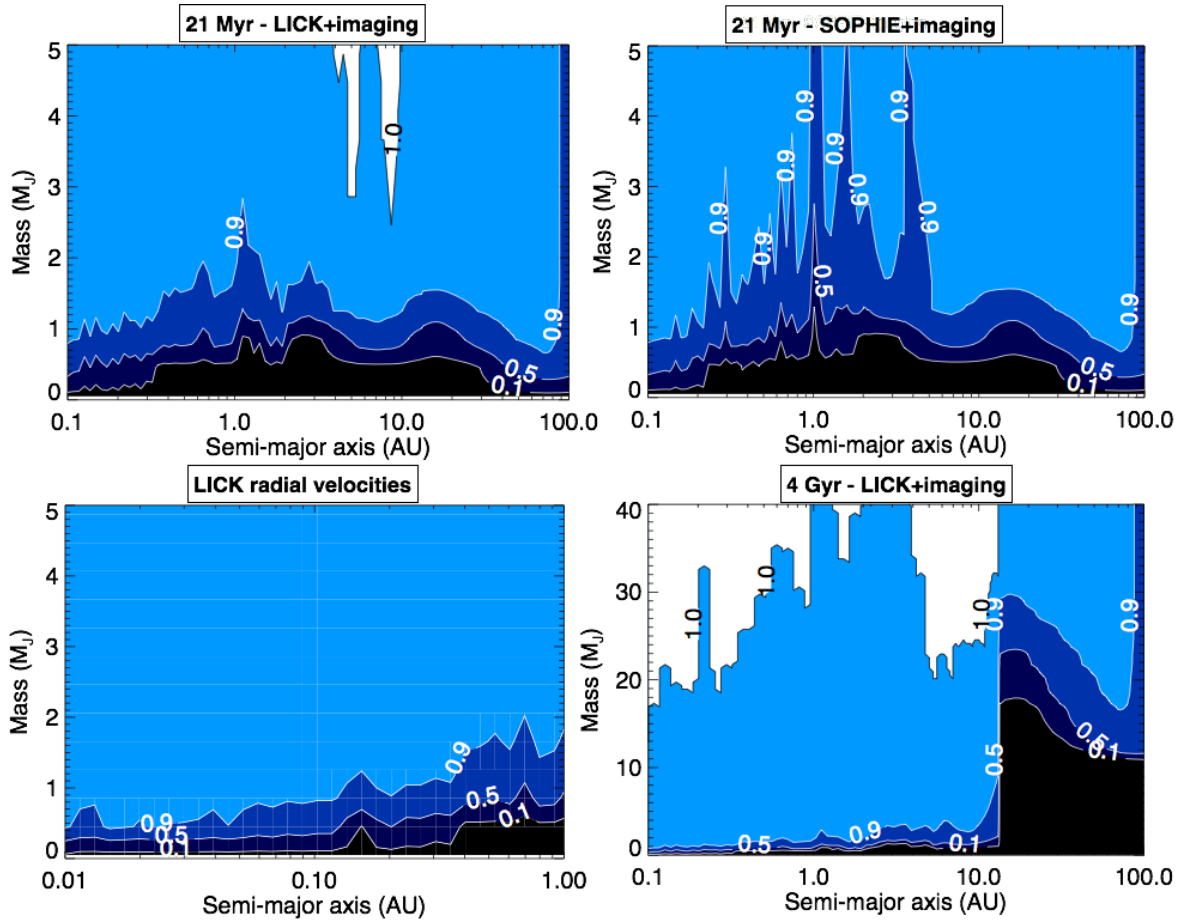

Fig. 19.

T_{obs}

T_{obs} T_{phot} (T_{phot} T_{spot}) p

M , R

2000

p

T_e

p

T_e p p 22%

T_e

T_e

T_e

T_e

T_e

p 7% p 22%

4

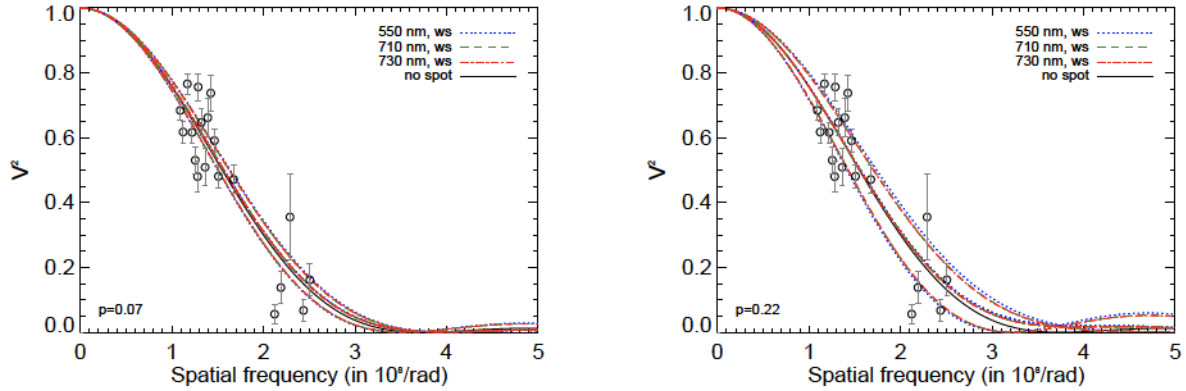

Fig. 20. Theoretical squared visibilities of a star without a spot (solid black line), and of a star with a spot (ws) as modelised with COMETS (Ligi et al. 2015). The different solid color lines represent the squared visibilities at different wavelengths and positions. The black circles represent the actual interferometric measurements (with error bars) of GJ504 performed with VEGA/CHARA. *Left panel*: a spot with a filling factor $p = 7\%$. *Right panel*: the same but for $p = 22\%$.

the theoretical visibilities of a star with a spot as modeled with COMETS at the different wavelengths and positions tested.

We find that a spot with $p = 7$ or 22% induces a change in the visibility curve which is still within the dispersion of measured values. Therefore, spots such as those considered here are not likely to have significantly biased GJ 504A's angular diameter measurement.

We, therefore, conclude that while spots may indeed be affecting the RVs, luminosity, radius, and $T_{\rm eff}$ estimates of GJ 504A, their effect is unlikely to bias all those quantities together by sufficient amounts and change the isochronal age estimates of the star.

8.2. Disentangling the atmospheric model solutions

We show in Fig. 21 the synthetic spectra in the *L*-*M* band and in the mid-infrared corresponding to the models fitting the presently available photometry of GJ 504b (Table 6; solutions with some pre-requisite on the companion radius). The **ATMO** and **Exo-REM** models predict very similar spectra distinctive from those corresponding to the Morley and **petitCODE** solutions. The difference arises from the non-equilibrium chemistry which is not considered in the case of the two latter models and modulates the strength of the CO_2 and CO absorption bands centered around 4.3 and 4.7 μm, respectively. Adaptive-optics *M*-band imaging from the ground should already tell whether the non-equilibrium chemistry is a pre-requisite for modeling the companion emission flux (model-to-model contrast between 1.16 and 1.48 mag in the *M*-band filter of the VLT/NaCo instrument). Coronographic imaging with the F430M and F460M filters of the Near Infrared Camera (NIRCam) on the *James Webb* Space Telescope (JWST) should also better constrain the shape of the 3.7–5 μm pseudo-continuum and could disentangle the **ATMO** and **Exo-REM** solutions.

Observations at longer wavelengths will be a niche for the Mid-Infrared Instrument (MIRI) of JWST. We can estimate that the contrast between GJ 504b and GJ 504A should range between 4×10^{-6} and 2.5×10^{-4} from 5 to 28.5 μm using the set of atmospheric models considered above and the SED of GJ 504A (Appendix A). The use of the four-quadrant phase masks together with ADI will be mandatory to reach GJ 504b contrasts and avoid saturation (Boccaletti et al. 2015). The four-quadrant phase masks can only be used jointly with the F1065C (λ_c = 10.575 μm, $\Delta\lambda$ = 0.75 μm), F1140C (λ_c = 11.40 μm, $\Delta\lambda$ = 0.80 μm), and F1550C (λ_c = 15.50 μm, $\Delta\lambda$ =

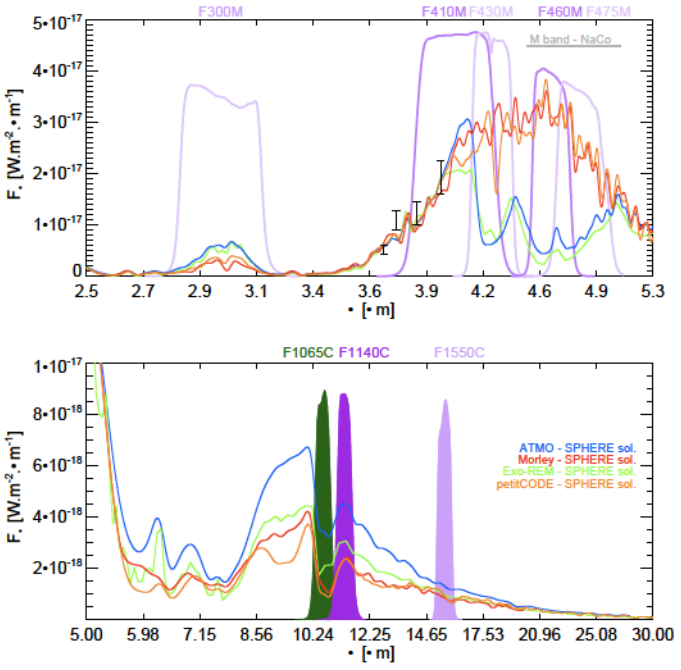

Fig. 21. Predicted apparent fluxes of GJ 504b in the near- and mid-infrared corresponding to the best-fitting synthetic spectra found in Sect. 5 with the G statistics and some knowledge of the object radius. The transmission of some key filters of JWST instruments are overlaid. We report the *L*-band photometry (Subaru/IRCS, LBTI/LMIRcam) of GJ 504b (black).

0.90 μm) filters. The MIRI photometry should enable to distinguish between the **ATMO** and **Exo-REM** solutions. The **Exo-REM** models indicate that the spectral slope between 11 and 15 μm probed by the F1140C- F1550C color should also be a good indicator of the percentage of the disk surface covered by clouds.

To conclude, we considered two representative solutions probing the log $g/[M/H]$ degeneracy in the posterior distributions shown in Figs. 8 and 9 at $T_{\rm eff}$ = 550 K. The spectra indicate that narrow and broad band photometry with JWST longward of 3 μm should not break the log $g/[M/H]$ degeneracy for all but the **ATMO** solutions. The MIRI data coupled to the SPHERE data points should nonetheless set stringent constraints (<100 K) on the $T_{\rm eff}$ based on our simulations and should allow for reduction of the error bar on the luminosity. The comparison of that

8.3. Formation pathway

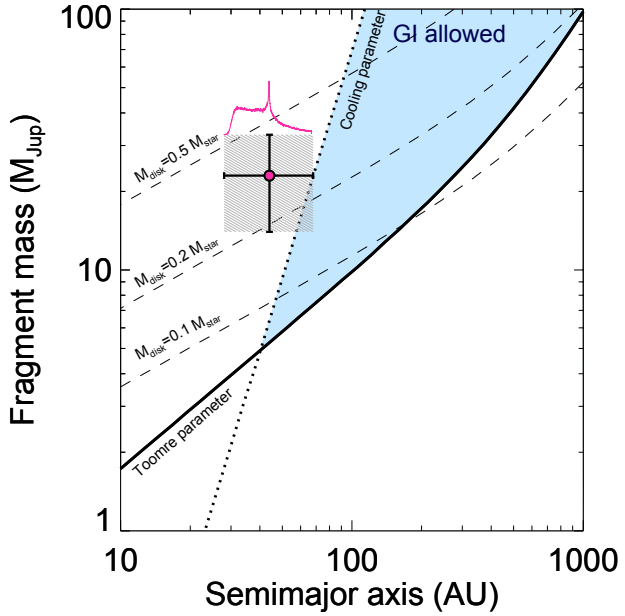

Fig. 22.

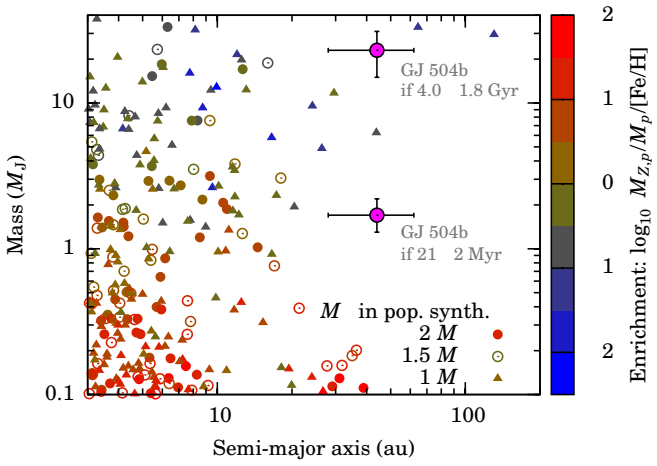

Fig. 23.

8.4. Finding analogs of GJ 504b with VLT/SPHERE

9. Conclusion

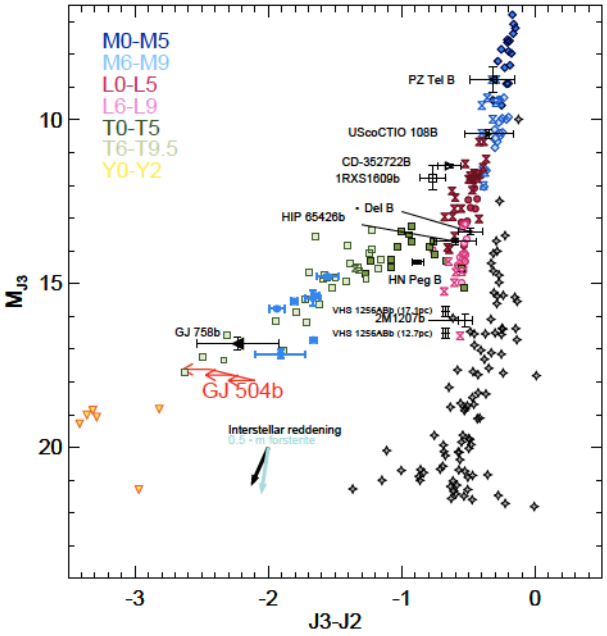

Fig. 24. Color-magnitude diagram exploiting the $J2$ and $J3$ photometry of SPHERE. We report the photometry of candidate companions detected around three SHINE targets with the DB_J23 filter of IRDIS (grey stars symbols). The reddening vector of 0.5 μm forsterite grains and the one corresponding to the interstellar extinction are overlaid (see Bonnefoy et al. 2016, for the details on how the vectors are computed).

the orbit of GJ 504b suggests that the system could have a spin-orbit misalignment. The radial velocity and imaging data allow exclusion of companions more massive than 2.5 and 30 $M_{\rm Jup}$ from 0.01 to 80 au assuming the young and old age range, respectively.

If GJ 504b is a brown-dwarf in an old system, we show that gravitational instability models possibly coupled to inward migration might explain its properties. Population synthesis models confirm that the core-accretion models can form such a massive object, but preferentially at semi-major axis shorter than 30 au. Both formation models would be challenged if the object is a planet with M = $1.3^{+0.6}_{-0.3}$ $M_{\rm Jup}$.

Additional key measurements could be obtained in the near future to better constrain the origins of the GJ 504 system. Additional astrometric monitoring of GJ 504b is crucially needed to (1) tighten down the posteriors on the inclination of GJ 504b orbit and confirm the spin-axis misaligment, and (2) constrain better the eccentricity. The latter could be related to the formation mechanism (see Ma & Ge 2014). JWST photometry and spectra of GJ 504b should yield the first robust constraints on the C/O, O/H, and C/H (or metallicity) ratios and on the importance of nonequilibrium chemistry in the atmosphere of GJ 504b. It will then become possible to compare the abundances to those of brown dwarfs (Line et al. 2017) and planets (e.g. Benneke 2015; Lavie et al. 2017). Deeper imaging data as gathered with the JWST should set stringent constraints on the probability of detection of companions beyond 80 au. Conversely, additional monitoring with SPHERE may carve the planet detection probability parameter space in the (15–30) au range where companions slightly more massive than GJ 504b may still reside if the system is old. Asteroseismology of the host star might enable us to close the debate on the system age. The more accurate luminosity and surface gravity of GJ 504b gathered by JWST might also enable the two possible isochronal ages for the system to be disentangled. *Gaia* may detect the wobble induced by GJ 504b over the duration of its nominal mission (5 yr) which could be used to exclude some of our orbital solutions and set upper limits on the companion mass.

To conclude, the J2J3 DBI filter of SPHERE offers good prospects for the detection and follow-up strategy of analogs of GJ 504b. Direct imaging surveys of nearby metal-rich G-type stars using this pair of filters would be of value to constrain the formation models.

Acknowledgements. The authors thank the ESO staff, the CHARA team, and the VEGA team for support in conducting the observations. M.B. is grateful to B. Burningham, G. Mace, D. Cushing, M. Liu, R.D. Rosa, D. Lafrenière, D. Kirkpatrick, A. Burgasser, J. Patience, B. Bowler, D. Lachapelle, E. Wright, and S. Leggett for providing the spectra of benchmark objects. We thank K. Rice, D. Forgan, and K. Todorov for fruitful discussions.This research has benefitted from the SpeX Prism Library (and/or SpeX Prism Library Analysis Toolkit), maintained by Adam Burgasser at http://www.browndwarfs.org/spexprism and from the Y Dwarf Compendium maintained by Michael Cushing at https://sites.google.com/view/ydwarfcompendium/. This research has made use of the SIMBAD database and VizieR catalogue access tool (operated at CDS, Strasbourg, France). This research has made use of NASA's Astrophysics Data System and of the Extrasolar Planet Encyclopedia (http://exoplanet.eu/). Part of the planet population of Fig. 23 is publicly available on DACE, the Data Analysis Centre for Exoplanets of the NCCR PlanetS reachable at https://dace.unige.ch. Additional populations will be added in future. DACE yields both interactive snapshots of the entire population at a given moment in time like the population-wide a–M or M–R diagrams as well as formation tracks of individual planets (e.g., $M(t)$, $R(t)$, etc.) for all synthetic planets. This publication makes use of VOSA, developed under the Spanish Virtual Observatory project supported from the Spanish MICINN through grant AyA2011-24052. This work is partly based on data products produced at the SPHERE Data Centre hosted at OSUG/IPAG, Grenoble. Data analysis was partially carried out on the open use data analysis computer system at the Astronomy Data Center, ADC, of the National Astronomical Observatory of Japan. SPHERE is an instrument designed and built by a consortium consisting of IPAG (Grenoble, France), MPIA (Heidelberg, Germany), LAM (Marseille, France), LESIA (Paris, France), Laboratoire Lagrange (Nice, France), INAF Osservatorio di Padova (Italy), Observatoire de Genève (Switzerland), ETH Zurich (Switzerland), NOVA (The Netherlands), ONERA (France), and ASTRON (The Netherlands) in collaboration with ESO. SPHERE was funded by ESO, with additional contributions from CNRS (France), MPIA (Germany), INAF (Italy), FINES (Switzerland), and NOVA (The Netherlands). SPHERE also received funding from the European Commission Sixth and Seventh Framework Programmes as part of the Optical Infrared Co-ordination Network for Astronomy (OPTICON) under grant number RII3-Ct- 2004-001566 for FP6 (2004-2008), grant number 226604 for FP7 (2009-2012), and grant number 312430 for FP7 (2013-2016). We also acknowledge financial support from the Programme National de Planétologie (PNP) and the Programme National de Physique Stellaire (PNPS) of CNRS-INSU in France. This work has also been supported by a grant from the French Labex OSUG@2020 (Investissements d'avenir – ANR10 LABX56) and from the Agence Nationale de la Recherche (grant ANR-14-CE33-0018). G.D.M. and C.M. acknowledge the support from the Swiss National Science Foundation under grant BSSGI0_155816 "PlanetsInTime". Parts of this work have been carried out within the frame of the National Center for Competence in Research PlanetS supported by the SNSF. This work is based upon observations obtained with the Georgia State University Center for High Angular Resolution Astronomy Array at Mount Wilson Observatory. The CHARA Array is supported by the National Science Foundation under Grant No. AST-1211929. J.H. is supported by the Swiss National Science Foundation (SNSF P2GEP2_151842). A.Z. acknowledges support from the CONICYT + PAI/ Convocatoria nacional subvención a la instalación en la academia, convocatoria 2017 + Folio PAI77170087.

References

Ackerman, A. S., & Marley, M. S. 2001, ApJ, 556, 872
Ahlers, J. P., Barnes, J. W., & Barnes, R. 2015, ApJ, 814, 67
Alibert, Y., Mordasini, C., & Benz, W. 2004, A&A, 417, L25
Alibert, Y., Mordasini, C., Benz, W., & Winisdoerffer, C. 2005, A&A, 434, 343
Alibert, Y., Carron, F., Fortier, A., et al. 2013, A&A, 558, A109

[illegible]

Appendix A: GJ504A SED and luminosity

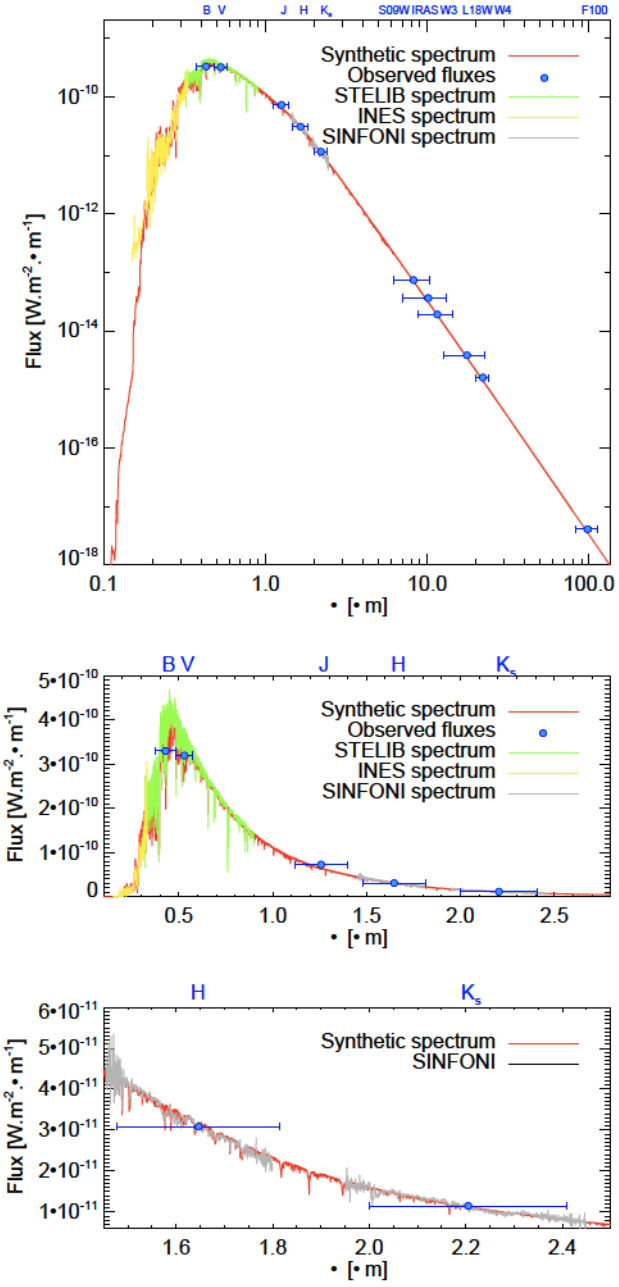

Fig. A.1. Photometry of GJ 504A (blue dots) compared to a BT-NEXTGEN synthetic spectrum (red line) at $T_{\rm eff}$ = 6200 K, log g = 4.5, and M/H = +0.3 scaled in flux. The flux-calibrated INES, STELIB, and SINFONI spectra (yellow, green, and grey lines, respectively) of the star are compatible with the flux-calibrated model-spectrum.

The magnitude of GJ 504A is unknown in the SPHERE passband. We, therefore, built a model of the star SED from the Johnson V and B band (Kharchenko et al. 2009), J, H, and K bands (Kidger & Martín-Luis 2003), AKARI S09W and L18W (Ishihara et al. 2010), IRAS 12 μm (Moshir 1989), WISE W3, and W4 (Cutri et al. 2014), and Herschel/PACS 100 μm (Moro-Martín et al. 2015) photometry[14]. That SED is well reproduced by a BT-NEXTGEN synthetic spectra (Allard et al. 2012b) with $T_{\rm eff}$ = 6200 K, log g = 4.5, and M/H = 0.3. Those parameters are the closest ones of the solution found by D'Orazi et al. (2017b) using high-resolution spectra. We confirm that no excess can be found up to 100 μm with our fitting solution. The flux-calibrated model spectrum reproduces equally well (Fig. A.1) the shape and flux of the STELIB medium-resolution ($R \sim$ 2000) optical spectrum (320–989 nm) of the star (Le Borgne et al. 2003) obtained in April 1994. We collected and averaged archival flux-calibrated UV spectra of the star from the "IUE Newly Extracted Spectra" (INES) database[15]. The spectra were collected with the LWR and SWP camera of the International Ultraviolet Explorer (Rodríguez-Pascual et al. 1999; Cassatella et al. 2000; González-Riestra et al. 2000, 2001) and have a reliable flux in the interval 150–331nm. We also reduced data of GJ 504A gathered with the SINFONI NIR integral field spectrograph (Eisenhauer et al. 2003; Bonnet et al. 2004) on June 9, 2014 (PI CACERES; Program 093.C-0500). The data were acquired with the H+K mode of the instrument yielding continuous medium-resolution ($R \sim$ 1500) spectra from 1.45 to 2.45 μm. The SINFONI data were reduced with the ESO data handling pipeline version 3.0.0 through the `Reflex` environment. Only one datacube, corresponding to a science exposure obtained at 02h41m04s UT, contained the star in the field of view. The star spectrum was extracted over a circular aperture with a radius of 325 mas. The spectrum was corrected from telluric absorption using the observation of the B9V star HD 141327 observed before GJ 504A. The 1.8–1.95 μm range was affected by telluric line residuals and was not considered any further. We flux-calibrated the spectrum using the K band flux from Kidger & Martín-Luis (2003). The H and K-band SINFONI spectrum is well reproduced by the BT-NEXTGEN model (Fig. A.1) and can be used to derive reliable IRDIS magnitudes of GJ 504A in the H2H3 and K1K2 channels (see below). We replaced the BT-NEXTGEN spectrum with the INES, STELLIB, and SINFONI spectra of GJ 504A and integrated the SED to estimate a log $L/L_\odot$ = 0.35 ± 0.01 dex. The error accounts for an uncertainty of 100 K on the $T_{\rm eff}$ of the BT-NEXTGEN model fit and for the uncertainty on the distance (0.08 pc; van Leeuwen 2007). The value is in good agreement with the one (log $L/L_\odot$ = 0.35 ± 0.05) derived by Fuhrmann & Chini (2015) from a V-band bolometric correction.

We used the spectrum of GJ 504A considered for the bolometric luminosity estimate and a spectrum of Vega (Mountain et al. 1985; Hayes 1985) to compute the photometric shifts between the J, H, and K photometry of GJ 504A and the

Table A.1. Apparent magnitude of GJ 504A in the IRDIS and HiCIAO CH_4 filters.

Band	Mag	Error
Y2	4.32	0.03
Y3	4.29	0.03
J2	4.18	0.03
J3	4.07	0.03
H2	3.87	0.03
H3	3.85	0.03
K1	3.79	0.03
K2	3.83	0.03
CH_4S	3.87	0.03
CH_4L	3.86	0.03

[14] The source is saturated in the WISE W1 and 2 images. The published *Spitzer* 70 μm photometry has large error bars (Sierchio et al. 2014) and was not considered in the fit. It confirms the lack of excess emission at 70 μm

[15] http://sdc.cab.inta-csic.es/ines/

Table A.2. [illegible]

[illegible]	[illegible]		[illegible]			[illegible]	[illegible] ($M_{\rm Jup}$)		[illegible]	[illegible]					$T_{\rm e}$		[illegible]		[illegible] bol)		[illegible]
[illegible]	T6.5	1.5	29.4	0.3	[illegible]	[illegible]			0.02	0.08	1.0	0.1	4.26	25	760	20	0.026	0.003	5.40	0.07	[illegible]
[illegible]	T7	1	15.76	0.09	[illegible]	[illegible]			0.18	0.05	...		4.3	0.5	741	25	[illegible]		...		[illegible]
[illegible]	[illegible]		14.1	0.4	[illegible]	[illegible]			0.04	0.08	0		[illegible]	[illegible]	[illegible]				5.18	0.06	[illegible]
[illegible]	[illegible]		11.06	0.04	[illegible]		66^{12}_{21}		[illegible]		[illegible]		$5.12^{0.09}_{0.17}$		726^{22}_{21}		[illegible]		5.60	0.05	[illegible]
[illegible]	[illegible]		5.84	0.03	[illegible]		31^{27}_{16}		0.05	0.17	[illegible]		$4.76^{0.27}_{0.28}$		714^{20}_{23}		[illegible]		5.55	0.05	[illegible]
[illegible]	[illegible]		17.2	0.2	[illegible]	[illegible]			0.38	0.06	...		5.0	0.3	680	55	[illegible]		5.83	0.05	[illegible]
[illegible]	[illegible]		11.7	0.2	[illegible]	[illegible]	[illegible]		[illegible]	[illegible]					695	60	[illegible]		5.62	0.03	[illegible]
[illegible]	[illegible]		12.5	0.8	[illegible]	[illegible]			0.24	0.09	[illegible]		5.0	0.3	560	30	[illegible]		6.01	0.05	[illegible]
[illegible]	[illegible]		5.79	0.01	[illegible]	[illegible]			0.2	0.4	[illegible]	[illegible]	[illegible]	[illegible]					5.21	0.04	[illegible]
[illegible]	[illegible]		8.29	0.15	[illegible]	[illegible]			0.32	0.05	...		[illegible]		[illegible]		[illegible]		6.11	0.05	[illegible]
[illegible]	[illegible]		15.8	1.0	[illegible]	...			0.64	0.17	0.5		[illegible]	[illegible]	[illegible]				...		[illegible]
[illegible]	[illegible]		41.7	0.9	[illegible]	[illegible]			0.20	0.04	...		[illegible]	[illegible]			$5.0^{1.3}_{1.7}$		...		[illegible]
[illegible] [illegible]	[illegible]		54.6	5.4	...	[illegible]	...				[illegible]	[illegible]	[illegible]				3		$5.51^{0.10}_{0.09}$		[illegible]
[illegible] [illegible]			9.3	0.4^{a}	...		7	4	...		...		4.0	0.3	600	30	0.3	0.4	...		[illegible]
[illegible] [illegible]			13.1	0.6^{a}	...		7	3	...		...		4.0	0.3	600	30	0.2	0.3	...		[illegible]
[illegible] [illegible]			36.0	2.4	...		...		...		...		[illegible]	[illegible]	[illegible]		...				4
[illegible] [illegible]			19	3^{a}	...		13	7	...		...		4.3	0.3	620	30	0.9	1.3	...		[illegible]

References. [illegible]

(a) [illegible] (b) [illegible]

Appendix B: Benchmark late-T objects

Appendix C: Details on the color–magnitude and color–color diagrams

Appendix D: Forward models exploring different C/O ratio

Appendix E: SOPHIE radial-velocity measurements

Table E.1.

		0 040			
		0 038			

300 K $T_{\rm e}$ 950 K 3 0 $\log g$ 5 5

1 0 $[M/H]$ 1 0

0 2 b(K_{zz} 8)

Appendix F: Magnitudes of ultracool companions predicted by Exo-REM

Table F.1. [illegible]

A G	M	M $M_{\rm Jup}$			[M H]			$Y2$			$Y3$			$J2$	$J3$	$H2$	$H3$	$K1$	$K2$
4	[illegible]	[illegible]	cloud	0 75	0		[illegible]	[illegible]	[illegible]	[illegible]	[illegible]	[illegible]	[illegible]	[illegible]					
4	[illegible]	[illegible]	cloud	0 75	[illegible]	[illegible]	[illegible]	[illegible]	[illegible]	[illegible]	[illegible]	[illegible]	[illegible]						
4	[illegible]	[illegible]	cloud	0	0		[illegible]	[illegible]	[illegible]	[illegible]	[illegible]	[illegible]	[illegible]	[illegible]					
4	[illegible]	[illegible]	cloud	0	[illegible]	[illegible]	[illegible]	[illegible]	[illegible]	[illegible]	[illegible]	[illegible]	[illegible]						
4	[illegible]	[illegible]	cloud	0 75	0		[illegible]	[illegible]	[illegible]	[illegible]	[illegible]	[illegible]	[illegible]	[illegible]					
4	[illegible]	[illegible]	cloud	0 75	[illegible]	[illegible]	[illegible]	[illegible]	[illegible]	[illegible]	[illegible]	[illegible]	[illegible]						
4	[illegible]	[illegible]	cloud	0	0		[illegible]	[illegible]	[illegible]	[illegible]	[illegible]	[illegible]	[illegible]	[illegible]					
4	[illegible]	[illegible]	cloud	0	[illegible]	[illegible]	[illegible]	[illegible]	[illegible]	[illegible]	[illegible]	[illegible]	[illegible]						
4	[illegible]	[illegible]	cloud	0 75	0		[illegible]	[illegible]	[illegible]	[illegible]	[illegible]	[illegible]	[illegible]	[illegible]					
4	[illegible]	[illegible]	cloud	0 75	[illegible]	[illegible]	[illegible]	[illegible]	[illegible]	[illegible]	[illegible]	[illegible]	[illegible]						
4	[illegible]	[illegible]	cloud	0	0		[illegible]	[illegible]	[illegible]	[illegible]	[illegible]	[illegible]	[illegible]	[illegible]					
4	[illegible]	[illegible]	cloud	0	[illegible]	[illegible]	[illegible]	[illegible]	[illegible]	[illegible]	[illegible]	[illegible]	[illegible]						
[illegible]	[illegible]	[illegible]	cloud	0 75	0		[illegible]	[illegible]	[illegible]	[illegible]	[illegible]	[illegible]	[illegible]	[illegible]					
[illegible]	[illegible]	[illegible]	cloud	0 75	[illegible]	[illegible]	[illegible]	[illegible]	[illegible]	[illegible]	[illegible]	[illegible]	[illegible]						
[illegible]	[illegible]	[illegible]	cloud	0	0		[illegible]	[illegible]	[illegible]	[illegible]	[illegible]	[illegible]	[illegible]	[illegible]					
[illegible]	[illegible]	[illegible]	cloud	0	[illegible]	[illegible]	[illegible]	[illegible]	[illegible]	[illegible]	[illegible]	[illegible]	[illegible]						
[illegible]	8	[illegible]	cloud	0 75	0		[illegible]	[illegible]	[illegible]	[illegible]	[illegible]	[illegible]	[illegible]	[illegible]					
[illegible]	8	[illegible]	cloud	0 75	[illegible]	[illegible]	[illegible]	[illegible]	[illegible]	[illegible]	[illegible]	[illegible]	[illegible]						
[illegible]	8	[illegible]	cloud	0	0		[illegible]	[illegible]	[illegible]	[illegible]	[illegible]	[illegible]	[illegible]	[illegible]					
[illegible]	8	[illegible]	cloud	0	[illegible]	[illegible]	[illegible]	[illegible]	[illegible]	[illegible]	[illegible]	[illegible]	[illegible]						
[illegible]	5	[illegible]	cloud	0 75	0		[illegible]	[illegible]	[illegible]	[illegible]	[illegible]	[illegible]	[illegible]	[illegible]					
[illegible]	5	[illegible]	cloud	0 75	[illegible]	[illegible]	[illegible]	[illegible]	[illegible]	[illegible]	[illegible]	[illegible]	[illegible]						
[illegible]	5	[illegible]	cloud	0	0		[illegible]	[illegible]	[illegible]	[illegible]	[illegible]	[illegible]	[illegible]	[illegible]					
[illegible]	5	[illegible]	cloud	0	[illegible]	[illegible]	[illegible]	[illegible]	[illegible]	[illegible]	[illegible]	[illegible]	[illegible]						
[illegible]	5	[illegible]	cloud	0 75	0		[illegible]	[illegible]	[illegible]	[illegible]	[illegible]	[illegible]	[illegible]	[illegible]					
[illegible]	5	[illegible]	cloud	0 75	[illegible]	[illegible]	[illegible]	[illegible]	[illegible]	[illegible]	[illegible]	[illegible]	[illegible]						
[illegible]	5	[illegible]	cloud	0	0		[illegible]	[illegible]	[illegible]	[illegible]	[illegible]	[illegible]	[illegible]	[illegible]					
[illegible]	5	[illegible]	cloud	0	[illegible]	[illegible]	[illegible]	[illegible]	[illegible]	[illegible]	[illegible]	[illegible]	[illegible]						
[illegible]	3	[illegible]	cloud	0 75	0		[illegible]	[illegible]	[illegible]	[illegible]	[illegible]	[illegible]	[illegible]	[illegible]					
[illegible]	3	[illegible]	cloud	0 75	[illegible]	[illegible]	[illegible]	[illegible]	[illegible]	[illegible]	[illegible]	[illegible]	[illegible]						
[illegible]	3	[illegible]	cloud	0	0		[illegible]	[illegible]	[illegible]	[illegible]	[illegible]	[illegible]	[illegible]	[illegible]					
[illegible]	3	[illegible]	cloud	0	[illegible]	[illegible]	[illegible]	[illegible]	[illegible]	[illegible]	[illegible]	[illegible]	[illegible]						
[illegible]	[illegible]	[illegible]	cloud	0 75	0		[illegible]	[illegible]	[illegible]	[illegible]	[illegible]	[illegible]	[illegible]	[illegible]					
[illegible]	[illegible]	[illegible]	cloud	0 75	[illegible]	[illegible]	[illegible]	[illegible]	[illegible]	[illegible]	[illegible]	[illegible]	[illegible]						
[illegible]	[illegible]	[illegible]	cloud	0	0		[illegible]	[illegible]	[illegible]	[illegible]	[illegible]	[illegible]	[illegible]	[illegible]					
[illegible]	[illegible]	[illegible]	cloud	0	[illegible]	[illegible]	[illegible]	[illegible]	[illegible]	[illegible]	[illegible]	[illegible]	[illegible]						